A Time Domain Phonon Pulse Fitting Analysis for the Cryogenic Dark Matter Search Experiment

by

Chandler Schlupf

Submitted to the Department of Physics
in partial fulfillment of the requirements for the degree of

Bachelor of Science in Physics

at the

MASSACHUSETTS INSTITUTE OF TECHNOLOGY

June 2014

Signature redacted

Author .....
Department of Physics
May 9, 2014

Signature redacted

Certified by .....
Professor Enectalí Figueroa-Feliciano
Thesis Supervisor, Department of Physics
Thesis Supervisor

Signature redacted

Accepted by .....
Professor Nergis Mavalvala
Senior Thesis Coordinator, Department of Physics

A Time Domain Phonon Pulse Fitting Analysis for the Cryogenic Dark Matter Search Experiment

by

Chandler Schlupf

Submitted to the Department of Physics
on May 9, 2014, in partial fulfillment of the
requirements for the degree of
Bachelor of Science in Physics

Abstract

Dark matter makes up 85% of the known matter in the Universe, but the exact nature of dark matter remains unknown. The Cryogenic Dark Matter Search experiment, CDMS, attempts to directly detect the leading candidate dark matter particle, the Weakly Interacting Massive Particle (WIMP), recoiling off of cold germanium crystals. When particles interact with the crystals' atoms, they produce two measurable signals: phonons and ionization. The phonon signal contains information about the event such as its type, energy, and position, and has a much better resolution for lower energy events than does the ionization, especially for nuclear recoils from WIMPs. Because of this, there is a strong motivation for extracting as much information as possible from the phonon signal. For my thesis, the raw phonon pulse signal in the time domain was fit to a functional form based on phonon physics within the crystal. The functional form was carefully checked using the Markov chain Monte Carlo method. A Boosted Decision Tree (BDT) was then used to analyze the parameters from the fits to determine how well the parameters could distinguish between event types such as nuclear versus electron recoil events, and surface versus bulk events. Cuts made on the data, from results of the BDTs that were analyzed with parameters from this time-domain fitting algorithm, yielded better descrimination power than ones that were analyzed with the parameters currently used by CDMS. Applying this method to data mimicking a 15 GeV WIMP distribution produced a 34.4% signal efficiency improvement over the values currently used by CDMS.

Thesis Supervisor: Professor Enectalí Figueroa-Feliciano
Title: Thesis Supervisor, Department of Physics

Acknowledgments

I would like to thank my thesis advisor, Professor Enectalí Figueroa-Feliciano. Besides guiding my project, he was always there to give me career and life advice when I most needed it. I appreciate him taking me on and giving me the chance to work with the amazing CDMS collaboration. In addition, my thesis would not be what it is without the enormous help of both Adam Anderson and Julien Billard. They truly went beyond their duty of graduate student and post doc in the time spent working with me on this project. They were available at a moments notice to explain a new concept in great length or look my work over. I hope to one day follow in their footsteps and be as good of a role model to undergraduates as they were to me.

I would also like to thank the Thesis Coordinator, Professor Nergis Mavalvala, who was my first semester Junior Lab professor. Junior lab was where I discovered my love for particle physics and data analysis. I was always excited for the discussions after my oral presentations with Professor Mavalvala because of her encouragement, kindness, and challenging questions.

I would like to give full appreciation to the funding from the UROP department and from the MIT Kavli Institute for supporting me while doing the research needed for this thesis. Lastly, I am grateful for all of the support I got from the MIT physics community, friends, and family. As many people know, MIT is not easy, and the motivation from all of these people were key to my success.

Contents

1 Introduction **9**

1.0.1 Dark Matter 9

1.0.2 The Cryogenic Dark Matter Search Experiment 14

1.0.3 Time Domain Pulse Fitting Analysis 16

2 Phonon Pulse Trace Physics **19**

2.1 Phonon Definition and Detection Method 19

2.2 Types of Phonons 20

2.2.1 Primary Phonons 20

2.2.2 Neganov-Luke Phonons 21

2.2.3 Relaxation Phonons 22

2.3 Phonon Discrimination Power 23

2.3.1 Nuclear Versus Electron Recoils 23

2.3.2 Surface Versus Bulk Events 24

3 Functional Form **27**

3.1 Parameter Restrictions and Initial Values 28

3.2 MATLAB Test and Comparison to Previous Research 28

4 Markov Chain Monte Carlo (MCMC) **33**

4.1 Introduction 33

4.2 MCMC Method Description 33

4.2.1 Probability Functions 34

4.2.2 Metropolis-Hastings Algorithm 34
4.2.3 Markov Chain Quality Selections 36
4.3 Implementation 36
4.4 Checks 37
4.4.1 Distribution Widths 38
4.4.2 Different Pulse Shapes 38
4.4.3 Variable Range 38
4.4.4 Different Noise Levels 39
4.4.5 Four Parameters Only 39

5 Implementation and Analysis **51**
5.1 Implementation into CDMS BatRoot 51
5.1.1 Speed 51
5.1.2 Data 53
5.1.3 Results 53
5.2 Boosted Decision Trees Analysis 54
5.2.1 Boosted Decision Tree Description 54
5.2.2 Results 56
5.3 WIMP Discrimination 61
5.4 Conclusion 62

Chapter 1

Introduction

1.0.1 Dark Matter

Evidence

It is known that the matter in the Universe is made up of approximately 15% baryonic matter and 85% dark matter [1]. This knowledge does not come from direct detection of dark matter, which has not yet occurred, but from indirect evidence within the universe, which can be seen on galactic, cosmological, and local scales.

The concept of dark matter was first introduced by Fritz Zwicky in 1933 when he studied the velocity dispersion of a group of galaxies in the Coma cluster [13]. He used the virial theorem, which in the case of a gravitational potential states $2\langle T\rangle = -\langle V\rangle$. The kinetic energy, T, can be obtained from the velocity dispersions. The potential energy, V, can be obtained using the approximate distance of galaxies from the center of the cluster, and the mass inferred by the light of the galaxies. He concluded that the mass density of the cluster needed to be significantly higher to produce the velocity dispersion he had observed.

The next piece of evidence was found looking at the Andromeda galaxy's velocity rotation curves. These are plots of the rotational velocity of the objects in the galaxy as a function of distance from the galactic core. Since most of the mass is in the core, it is expected that objects near it will be moving faster than objects farther away from it. This can be seen by looking at the force equation: $F = \frac{mv^2}{r} = \frac{GmM}{r^2}$,

where m is the mass of the moving object, v is its velocity, r is the distance from the mass M, and G is the gravitational constant. This equation yields $v = \sqrt{\frac{GM(r)}{r}}$, a velocity which falls with the square root of the radius beyond the visible galactic disk where the luminous matter is contained. However, it was found that the rotational velocities of objects were actually approximately constant as a function of radius out to the largest r where the rotation curve can be measured, see Figure 1-1 for an example. One interpretation of this is that there is a halo of non-luminous (dark) matter extending beyond the luminous matter seen in the galaxy.

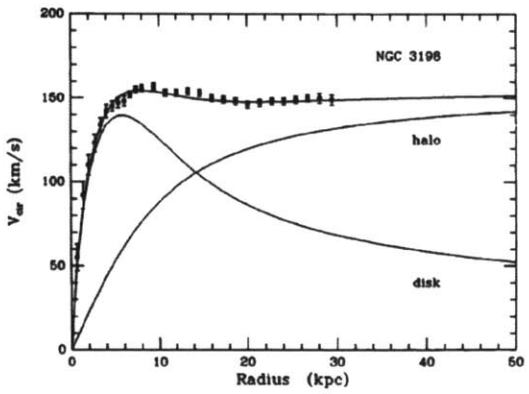

Figure 1-1: A rotation curve found in 1989 for the galaxy NGC3198. At about 10 kpc, the edge of the luminous mass of the galaxy, the velocity distribution would be expected to begin to fall with the square root of the radius, but instead it is seen to be relatively constant. The dark matter halo and luminous disk contributions are plotted as lines which add up to the observation. [4]

Another large piece of evidence comes not from observing galaxies, but from cosmology and the observation of the cosmic microwave background (CMB) radiation. The CMB is uniform to 1 part in 10^5 [6]. The anisotropies are attributed to acoustic oscillations in the photon-baryon plasma before the CMB was emitted and before diffusion damping. Both ordinary baryonic matter and dark matter interact gravitationally with the plasma, but only baryonic matter interacts with the photons. This means these two types of matter had different effects on the oscillations of the plasma. A power spectrum of the anisotropies of the CMB, Figure 1-2, yields peaks which tell us about the Universe. The first and third peak tell us the baryonic matter and dark matter density, respectively. They reveal the 85% dark matter and 15% baryonic

matter composition of the Universe.

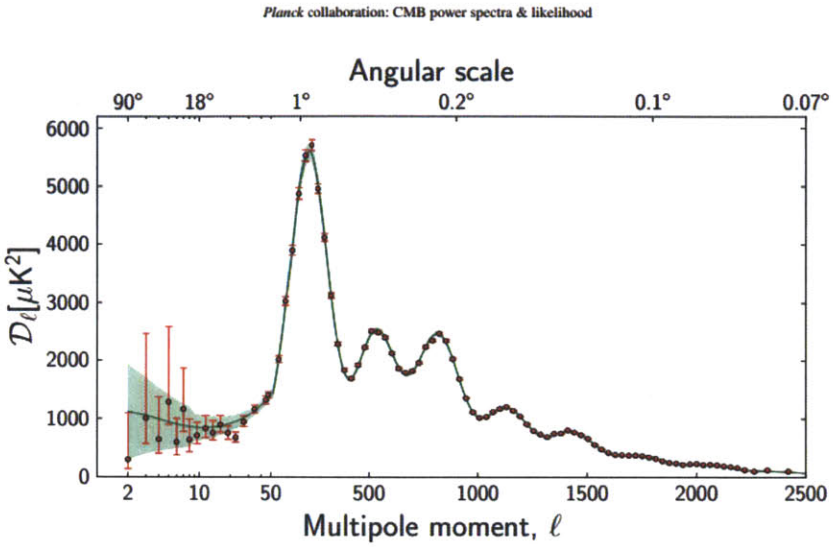

Figure 1-2: The power spectrum of the CMB based on 2013 Planck data. The first and third peak tell us about the density of baryonic and dark matter. [3]

A piece of evidence which is now considered one of the most compelling pieces is the bullet cluster, Figure 1-3. This is a galaxy cluster that relatively recently collided with another cluster. The gas forming most of the cluster's mass was seen to decelerate after the collision. However, the total mass of the system, which can be deduced by gravitational lensing studies, was seen to continue moving after the collision without deceleration. The comparison of the luminous matter to where the majority of the gravity of the system is located poses a challenge to the theory of modifications of the gravitation force law. It also confirms that dark matter is weakly interacting, unlike the luminous matter.

Figure 1-3: The bullet cluster of galaxies colliding. The pink shows the baryonic matter of the cluster, while the blue shows the gravity (aka dark matter) of the cluster. [4]

Through galaxy cluster mass densities, galaxy rotation curves, the cosmic microwave background, the bullet cluster, and many more observations, the evidence for dark matter is overwhelming. The next important step for scientists is to determine the composition of dark matter.

Candidate Particles

Any dark matter candidate must have several key properties in order to satisfy observational constraints. First, evidence from the CMB indicates that dark matter is, at least primarily, not composed of baryonic matter. Second, the large scale structure of the Universe indicates that dark matter must be cold, or slowly moving. Dark matter cannot be moving at relativistic speeds and make the structures we observe. Next, dark matter must be stable for at least the time scale of the current age of the Universe. This is known through the observation of a non-varying total dark matter mass fraction. Another important fact about dark matter is that it interacts very weakly. The bullet cluster exemplifies this because it is clear that the baryonic gas interacts and collides with itself, whereas the dark matter passes through the baryonic matter and its distribution is undisturbed. Dark matter also clearly interacts extremely weakly with electromagnetic radiation, hence the name dark. [8]

Using all of this information, there are a variety of suitable particle candidates for dark matter.

- **Black Holes**: Black holes that could have formed in the early universe, called primordial black holes, would be very difficult to detect unlike extremely large black holes such as the one at the center of the Milky Way. The formation of these types of black holes in numbers large enough to account for dark matter is only possible in certain cosmological models. An experiment which looks for these black holes, called MACHO, has found them to be a very unlikely candidate for dark matter.

- **Axions**: The strong CP problem is the question of why QCD has not been observed to break CP symmetry. Peccei and Quinn proposed a solution for this problem, which involves the spontaneous breaking of a new U(1) symmetry, creating a bosonic particle called the axion. Axions would be produced as cold particles in the early universe, and would need to have a mass of around 10μeV to agree with the dark matter density of the universe.

- **Neutrinos**: Neutrinos are non-baryonic matter that definitely makes up at least some part of the non-baryonic mass of the universe in the form of radiation. Standard model neutrinos have been observed, and there is also the possibility of another type of neutrino called the sterile neutrino. Standard model neutrinos, however, are extremely light, and also relativistic, therefore are not a good candidate for dark matter. Specific models of the sterile neutrino involve a non-thermally produced keV neutrino.

- **WIMPs**: The weakly interacting massive particle (WIMP) is a hypothetical particle which has coupling strengths on the order of the weak scale, and has a mass roughly between 10GeV and 10TeV. This model for dark matter is supported by both particle physics and cosmology, and is currently the leading candidate. From physics of the early universe, a density of $\Omega_{DM}h^2 \approx .1$, where h is the Hubble constant, is predicted for cold dark matter, which is comparable to the current observation of $\Omega_{DM}h^2 = 0.1198 \pm 0.0026$ [8]. From particle

physics, new supersymmetry particles are again on the weak scale, and are therefore WIMP candidates.

Because WIMPs are the leading candidate, there are a very large number of experiments searching for these types of particles. There are multiple categories of detection: indirect detection, direct detection and production.

Production has the potential of happening at the Large Hadron Collider (LHC), where new particles found in the future with the described characteristics could be WIMP candidates.

Indirect detection experiments look for products of WIMP annihilations. WIMP particles are potentially Majorana particles, meaning that they are their own antiparticle. This would cause high-density regions of WIMPs to annihilate with each other and produce either gamma rays or particle anti-particle pairs. There are many telescopes currently looking for this signal.

There are also many experiments aimed at directly detecting dark matter. These experiments are looking for signs of a WIMP particle scattering off of nuclei in their detectors. I will now discuss in more detail how this is done by introducing the experiment I am working on, CDMS.

1.0.2 The Cryogenic Dark Matter Search Experiment

The Cryogenic Dark Matter Search experiment, CDMS, is searching for WIMPs through direct detection [2], [9]. CDMS II, the second phase of CDMS, was located in the Soudan Underground Mine in Soudan, Minnesota. Because it was far underground, the Earth could be used as a shield to block a large amount of the cosmogenic background.

The goal of CDMS is to search for WIMPs by recording and analyzing information from particles interacting with detectors, more specifically recoiling off of the detectors' atomic nuclei and electrons. The most important information that is obtained is the energy of the event, the location within the detector, and the type of the recoiling particle.

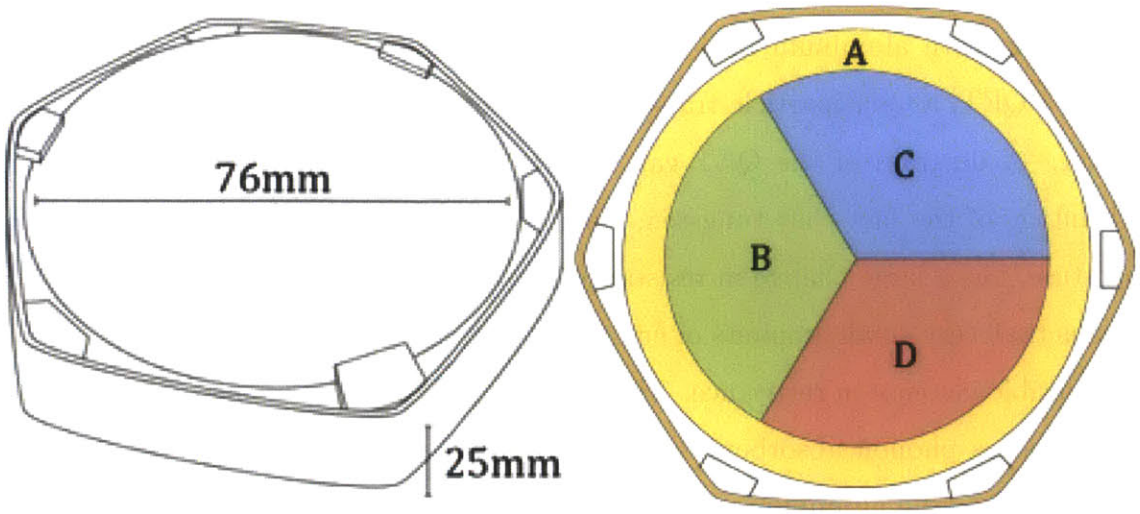

Figure 1-4: A diagram of the CDMS iZIP detector. The left side shows the dimensions and shape of the detector. The right side shows the phonon channel configuration for one face of the detector. [2]

CDMS detectors are 600g germanium crystals designed to have the ability to detect phonons, the vibrations in the crystal caused by recoiling nuclei, and ionization, the charge carriers stripped from crystal atoms during an event. They are located in a cryostat maintained at 50mK. It is important that they are kept at such a cold temperature because temperature relates to the experiment's sensitivity and functionality. The low temperature keeps the superconducting sensors at their critical temperature, and is also required so that the thermal energy in the crystals carried as phonons does not overpower the phonon energy coming from very low energy events.

The specific detectors used by CDMS are called interleaved Z-sensitive Ionization Phonon detectors (iZIP). They are stacked into 5 towers of 3 detectors. Each iZIP detector has 8 phonon sensors or channels, 4 on each side, and 4 ionization channels, 2 on each side. The configuration can be seen in Figure 1-4.

The iZIP ionization sensors on the faces of the detectors are electrodes. When a particle interacts with an atom in the germanium crystal, it can impart enough energy to create electron-hole pairs. A voltage bias is set up across the detector, causing the electrons to be collected on one side, and the holes to be collected on the other.

iZIP detectors measure phonons using a technology called transition-edge sensors (TESs), photolithographically patterned on the top and bottom surfaces of the crys-

tals, along with aluminum fins. This system of TES sensors and aluminum fins is called a QET, a Quasiparticle-trap-assisted-Electrothermal-feedback Transition-edge sensor. A diagram of the QET can be seen in Figure 1-5. TESs work by taking advantage of the fact that tungsten, when kept at its superconducting critical temperature, has a large change in resistance due to small changes in temperature. This means that very small amounts of energy, or increases in temperature, can produce a measurable increase in resistance. The small amount of energy comes from aluminum fins, used as phonon absorbers, which surround the TES sensors. When a phonon is incident on the aluminum, a Cooper pair is broken up and the phonon energy is transfered to the electrons. When the electrons reach the tungsten strip, it is kept at its critical temperature by a feedback loop which creates the signal.

The signal the iZIP detectors create for an event is a phonon pulse, which can be further analyzed, along with the charge information, to learn about the event characteristics.

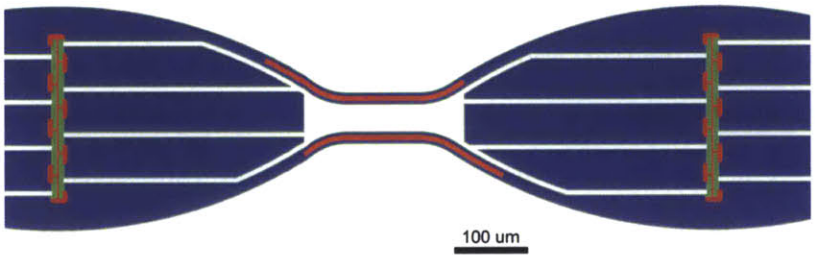

Figure 1-5: Diagram of the QET, where blue is the aluminum and red is the tungsten strips. [4]

1.0.3 Time Domain Pulse Fitting Analysis

My thesis analyzes the shape of the pulse created by the phonon signal in the time domain in order to distinguish the event type and the event location of low energy events. A generalized functional form to model the data was thoroughly tested by analyzing its likelihood distribution via the MCMC (Markov Chain Monte Carlo) algorithm. Once the 9-parameter functional form was checked, it was implemented into the CDMS BatRoot software, which takes the raw data from the detectors and outputs reduced quantities (RQs). These results were then analyzed using a Boosted

Decision Tree to determine how the RQs could be used to discriminate event types.

A thorough description of the underlying phonon physics within the detector, the choice of functional form, the MCMC algorithm, and the implementation results follow.

Chapter 2

Phonon Pulse Trace Physics

2.1 Phonon Definition and Detection Method

Phonons are excitations of the vibrations of the crystal lattice atoms, and are often referred to as quasi-particles. A quasi-particle is a phenomenon that occurs in a solid when excitations behave as if they are weakly interacting particles in free space [12]. In the CDMS detectors, motion of nuclei or of charge carriers within the crystal can cause these excitations. Phonon data is used to measure the energy of events with good resolution, and is used to determine the position of the event in order to reject background events. There are two types of phonons: thermal and athermal. Thermal phonons measure the overall temperature of the crystal after it has equalized. Athermal, or local phonons, effectively are local temperature changes, and require measurements very soon after the event before they have relaxed into the crystal. CDMS measures these local phonons. Athermal phonons become thermal on a time scale of $100 - 200\mu s$. The QET's in the CDMS detector have a readout, or a rate of measurement, of $1.6\mu s$, and are sensitive to changes on the scale of $10 - 20\mu s$. These values are much smaller than the athermal phonon time scale, so the sensors are able to pick up these local phonons. Understanding the propagation physics of these initial athermal phonons, referred to simply as phonons for the rest of the discussion, determine how well we understand the position of the event.

Phonons with high energies scatter often as they travel through the detector, and

therefore have a short mean free path length, which is the average length a particle travels between successive collisions. This causes high energy phonons to follow quasi-diffusive propagation. Quasi-diffusive propagation is diffusive propagation, a random walk, with an increasing mean free path length. As phonons travel, they anharmonically decay, which is when phonons decay into lower energy phonons. While traveling and losing energy, they slowly becoming more and more ballistic, essentially traveling in a straight line through the crystal because their mean free path is on the order of the size of the crystal.

The phonons bounce around the crystal until they are absorbed by a QET on the top or bottom surfaces of the detector. Only 6.1% [10] of the surface is covered by these sensors, so when phonons hit the surface they are more likely to simply reflect off and continue traveling. The more phonons bounce off the surface, the more likely it is that they will eventually be absorbed. Therefore, the rate at which they are absorbed by a QET is approximately proportional to the rate at which they bounce off of the surface. That means that short mean free path length, high energy phonons, when they end up near a surface, will be absorbed relatively quickly because they will most likely bounce off of the wall multiple times in their random walk before becoming ballistic. Long mean free path length, lower energy phonons however, after bouncing off of the wall, will likely travel the length of the detector before hitting another wall, slowing down the rate at which they bounce off of surfaces, and therefore slowing down their absorption rate.

2.2 Types of Phonons

2.2.1 Primary Phonons

When a particle scatters off of the nucleus of a crystal atom, high energy phonons called primary phonons are created. If the scattering event happens in the bulk of the detector, since the phonon loses energy as it travels and lengthens its mean free path length, it is absorbed more slowly by the sensors. If this scattering event happens near the surface of the detector, the phonons will be absorbed quickly because of their

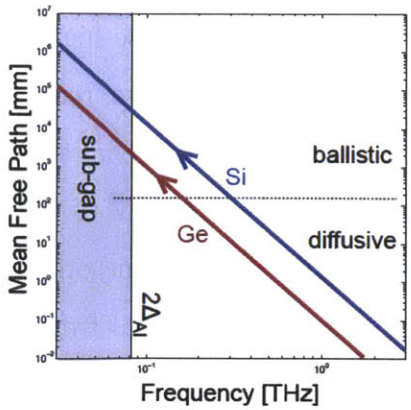

Figure 2-1: Phonon energy relationship to mean free path length. Two detector materials, germanium (CDMS II material) and silicon, are shown. Phonons travel left and upwards on these lines as they lose energy traveling around the detector. There is a mean free path length cut off where the phonons become ballistic. The gap is where the phonons no longer have enough energy to break the Cooper pairs in the aluminum fins on the QET, and are therefore no longer detected.
[11]

high energy. This results in a quick rise time for the pulse in the time domain when the event is near the surface, and a relatively slower rise time when the event is in the bulk, as can be seen in some example pulses in Figure 2-2.

2.2.2 Neganov-Luke Phonons

When a nuclear recoil event occurs, about 30% of the energy goes into motion of the nucleus' surrounding charge carriers (electrons or holes). Charge carriers can also be put into motion by interaction with charged particles traveling through the crystal. Since the crystal is set up with a voltage across it, the electrons which have been put into motion are accelerated towards one detector surface, and the holes are accelerated towards the other surface. As they both accelerate, they scatter off of other crystal atoms, losing energy in the form of another type of phonon, the Neganov-Luke phonon, or Luke phonon for short. The Luke phonon energy is the ionization energy multiplied by the change in voltage, and the voltage drop in the crystal is greatest near the surfaces. Therefore, the majority of the production of Luke phonons happens near the surfaces as the charge carriers radiate away the

energy gained from the change in voltage. These high energy phonons created near the surface are absorbed at a relatively quick rate, reflected by the fact that electron recoil events have a quicker rise time than nuclear recoil events (see Figure 2-2). If the original scattering event happens in the bulk of the detector, the electrons will travel to one side, and the holes will travel to the other side, accelerating along the way and yielding a relatively even phonon signal from sensors on both sides of the detector. If the scattering event happens near the surface however, the form of the electric field in the detector causes both the electrons and holes to be accelerated to the surface they are near (see Figure 2-3). This causes a large Luke phonon signal on that side of the detector and a minimal one on the other side.

2.2.3 Relaxation Phonons

When the charge carriers hit the band structure of the metal walls, they can relax back down into the metal's zero energy state from their excited state. The released energy is in the form of a phonon, called a relaxation phonon. These are low energy, and therefore already ballistic phonons, and are slowly absorbed by both sides of the detector having no discrimination power.

The equation for the total phonon energy is:

$$P_{total} = P_{primary} + P_{relax} + P_{luke} = E_{recoil} - P_{relax} + P_{relax} + P_{luke} = E_{recoil} + P_{luke} \quad (2.1)$$

The energy of the primary phonons is the total energy from the recoil event minus the energy used to ionize the atoms, but this energy is gained back later when the charge carriers relax into the metal's zero energy state. These values cancel out, and because the relaxation phonons did not have any discrimination power anyway, they can be ignored during the analysis.

2.3 Phonon Discrimination Power

The goal of the CDMS experiment is to be able to determine if there is a WIMP event among the events from other particles hitting the detector. In order to do this, we must be able to use the data collected, the charge and phonon information, to distinguish between different types of events. A summary of the phonon pulse shapes for different event types can be seen in Figure 2-2.

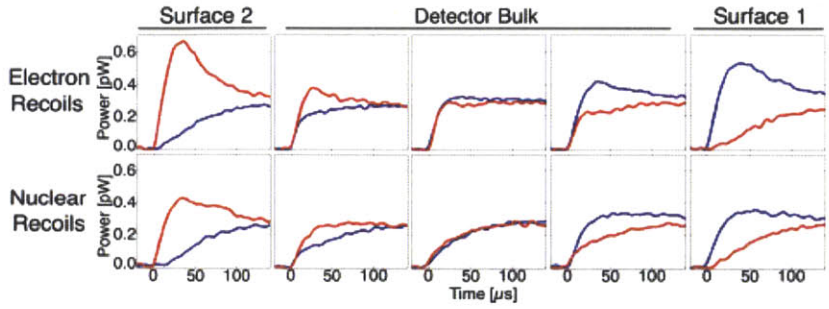

Figure 2-2: Examples of real phonon pulses from different event types and event locations. The signal received by surface 1 of the detector is in blue, and the signal received by surface 2 is in red. [10]

2.3.1 Nuclear Versus Electron Recoils

The primary discrimination power between nuclear and electron recoils is comparing the phonon energy and the charge energy. In the case of an electron recoil, there will be much more charge motion, and less primary phonon creation than compared to a nuclear recoil. This causes the yield, or the ratio of charge signal to phonon signal, to be approximately one in the case of electron recoils. In nuclear recoils however, there is a much larger phonon signal relative to the charge signal and the ratio is less than one.

Nuclear and electron recoils can also be distinguished by just looking at the phonon signal. The phonon signal is a pulse, which is a combination of the three types of phonons. The pulse shape will be different for different event types and locations. For an electron recoil, the majority of the phonons created are Luke phonons. This causes a pulse with a quicker rise and a more peaky appearance than a nuclear recoil

pulse, reflecting the faster absorption of the phonons. Using yield to discriminate between electron and nuclear recoils fails at low energies because of the resolution of the experiment in this regime. Phonons, however, have a much better resolution than charge at these energies, so using the phonon pulse information can further improve discrimination power.

2.3.2 Surface Versus Bulk Events

Surface events in the detector are considered unreliable. The main reason for this is because background beta particles have a lower yield when within about $10\mu m$ of the surface, which causes them to look like nuclear recoil events. Because we don't want to mistake one of these background beta events for a potential WIMP nuclear recoil signal, surface events are thrown out. Being able to distinguish between whether an event occurs near the surface or in the bulk of the detector is therefore very important.

One way CDMS distinguishes between surface and bulk events is by comparing the charge collection on each side of the detector. The voltage layout of the detector can be seen in Figure 2-3. Both the electrons and holes of events occurring in the light red region of the figure are collected on the same side, causing one side to see a charge signal and the other to see none in the case of a surface event. Because there is in general less charge collection from surface events, low energy events (<8keV) do not provide enough of a charge signal to be able to distinguish between surface and bulk events. Because phonons still have a decent resolution at these low energies, they potentially can be used to further discriminate.

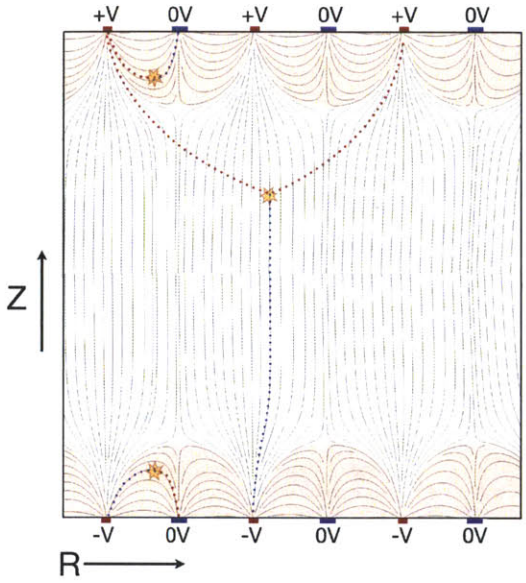

Figure 2-3: Voltage lines for a cross section of the detector. Z is the vertical position variable, R is the radius variable, and V is the voltage.

The primary phonons created near the surface of the detector are absorbed at a quicker rate than ones created in the bulk of the detector, causing the pulse rise to be sharper for surface events. Also in the case of a surface event, Luke phonons will cause one of the surfaces of the detector to have a much larger and peakier signal than the other side of the detector. These two features can be used to distinguish a surface event from a bulk event.

Events that occur at high radius near the side walls can be distinguished because they also cause the outer phonon sensor channels to have a larger Luke phonon signal. These events are problematic because charge carriers can get trapped in the side wall. This causes their yield to be lower, making them look like nuclear recoils. These are therefore regarded as background events and are thrown out so they can not be mistaken for a nuclear recoil WIMP signal.

Chapter 3

Functional Form

The physics of the primary and Luke phonons is the motivation behind the functional form used when trying to fit the phonon pulse shape. The functional form is the sum of two double exponential pulses, each with a rise time and a fall time. One of the pulses represents the quasi-diffusive and Luke phonons, and has a subscript f for fast. The other pulse represents the ballistic phonons, and has a subscript s for slow. The parameters of the function were:

1. A_f and A_s: amplitudes describing the height of each pulse.

2. T_f and T_s: time offsets describing the start of each pulse.

3. R_f and R_s: rise time constants describing the speed at which the phonons of each type get absorbed, as well as the response time of the TES.

4. F_f and F_s: fall time constants describing the time scale for energy to be absorbed by the TESs and thermalized into the cold bath of the dilation refrigerator.

5. $Shift$: a vertical shift accounting for any overall DC offset of the entire pulse coming from the readout electronics.

The equation for the functional form is then given by:

$$f(t) = H(T_f) \cdot [A_f \cdot (1 - e^{-(t-T_f)/R_f}) \cdot e^{-(t-T_f)/F_f}]$$
$$+H(T_s) \cdot [A_s \cdot (1 - e^{-(t-T_s)/R_s}) \cdot e^{-(t-T_s)/F_s}] + Shift.$$

H represents the Heaviside function, allowing each pulse to start at the designated time offset.

Because the surface, bulk, electron recoil, and nuclear recoil events all have characteristic features (see Figure 2-2), knowing the functional parameters of the pulse can possibly be used to distinguish the event type.

3.1 Parameter Restrictions and Initial Values

Fitting was first tested in MATLAB (described more in Section 3.2). It was found that fits converged well for a large variety of different initial values. The ones chosen are summarized in Table 3.1. All values have fixed initial conditions except for the amplitudes and the overall vertical shift. For the two amplitudes, A_f and A_s, the total pulse amplitude is extracted from the data and divided by two for each initial condition. For the vertical shift, $Shift$, the average value of the last 5% of the trace is taken as an approximate baseline for the pulse.

The units on the table shown are in microseconds. The pulse is read out in time bins, where each time bin is $1.6\mu s$, the sampling rate of the readout equipment. Each trace consists of about $6553\mu s$, or 4096 bins of data. The first approximately 512 bins is pre-trigger information from about $820\mu s$ before the pulse was detected. This can be visualized in the simulated pulse seen in Figure 3-1.

3.2 MATLAB Test and Comparison to Previous Research

The time-domain fitting of the phonon pulses of the CDMS II experiment were first performed as part of Scott Hertel's PhD thesis [11]. A conference proceeding describ-

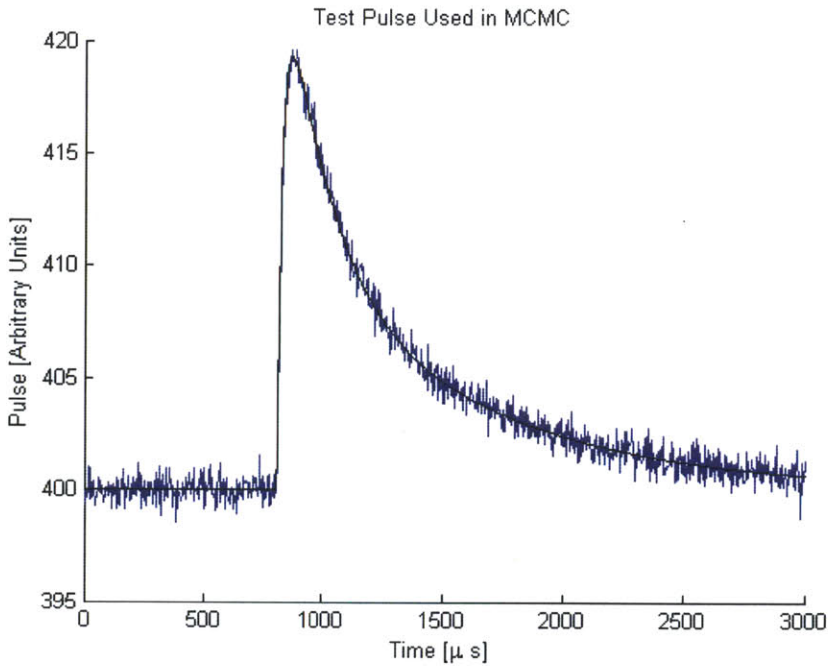

Figure 3-1: A simulated pulse with noise corresponding to an energy of approximately 30keV. The range is from 0 to 3000 μs, cutting off the tail of the trace. The parameter values in μs, are: $A_f = 15$, $T_f = 809$, $R_f = 20$, $F_f = 150$, $A_s = 8$, $R_s = 84$, $F_s = 755$, $Shift = 400$.

Parameter	Initial Value	Lower Bound	Upper Bound
A_f	Half of pulse height	0	10 times initial value
T_f	800	500	1000
R_f	20	0	200
F_f	100	0	400
A_s	Half of pulse height	0	10 times initial value
T_s	805	0	50
R_s	90	0	400
F_s	700	500	1200
$Shift$	Mean of pre-pulse noise	0	10^5

Table 3.1: A table giving the values used for fitting the pulses given in microseconds.

ing his efforts can be found in this source: [10]. To summarize, he used an identical functional form as the one described in this section, the only exception being he did not have an overall DC Shift variable. In addition, he fixed F_s to 755 μs when performing the fits.

In attempting to discriminate between electron recoils and nuclear recoils, quanti-

ties obtained from the fits were compared. The first quantity obtained was rise time, defined when the curve first hits some percentage of the total height. Hertel used the time it took for the pulse to go from 40% to 70% of the total height. The four summed traces of each side of the detector were compared in order to determine how well they discriminated between electron and nuclear recoils. This was motivated by the fact that electron recoil rise times are typically faster than nuclear recoil rise times, as can be visualized in Figure 2-2. In addition, he compared a quantity "radius", defined by: $[(40\% \text{ to } 70\% \text{ rise of side } 1)^2 + (40\% \text{ to } 70\% \text{ rise of side } 2)^2]^{1/2}$, for each type of recoil.

I implemented the fitting in MATLAB using a least squares curve fitting method. The bounds used were slightly tighter than the ones in Table 3.1, but the initial conditions were the same. This method was actually extremely robust, and the initial conditions did not seem to change the resulting fit much. I tested this fitting method using real events from the detectors. Two representative examples of real data pulses and their fits can be seen in Figure 3-2. These plots provided a nice visual reassurance that the fit was working well both at high and low energies.

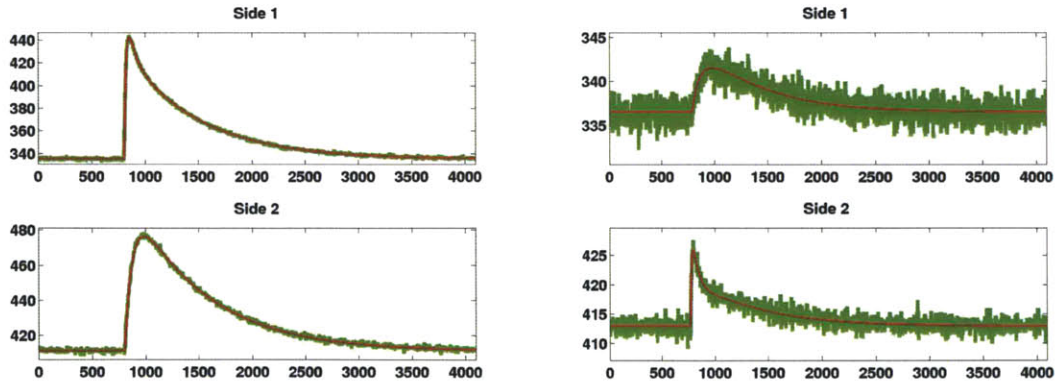

Figure 3-2: A high energy event on the left, and a low energy event on the right. The real pulse data is shown in green, and the fit is overlaid in red.

After I implemented the fitting in MATLAB using a least squares curve fitting method, my results were compared with Hertel's to see if they produced roughly the same discrimination power. I calculated the rise time and radius quantities for both electron and nuclear recoil data, and compared the resulting plots to the ones made by Hertel, which can all be seen in Figures 3-3 and 3-4. Hertel's plots show how the rise

time and radius quantities can be used to distinguish, to a certain accuracy, between electron and nuclear recoils. My results were qualitatively consistent with Hertel's, but the discrimination was not quite as strong. This is for a variety of reasons, including the fact that I used a small sample size, the data set was different, and I don't have specific information about his implementation and goodness of fit. These qualitatively consistent results were encouragement to proceed to a more rigorous implementation of this analysis method.

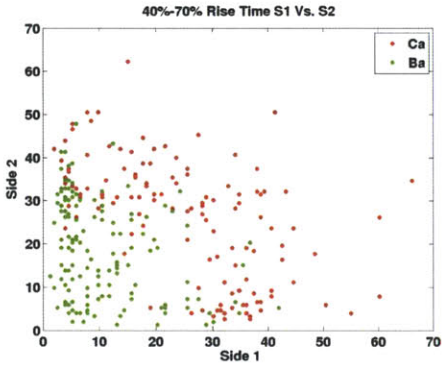

(a) 40%-70% rise time distribution of the summed side 1 and side 2 pulses using my MATLAB fitted pulses, energy range apprimately 10-20keV.

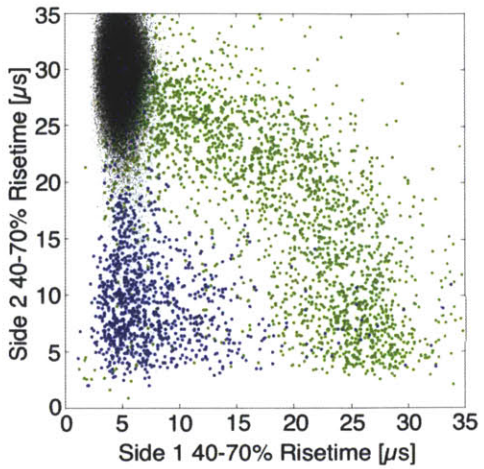

(b) 40%-70% rise time distribution of the summed side 1 and side 2 pulses as found by S. Hertel and M. Pyle. Bulk electron recoils are blue, bulk nuclear recoils are green, and side 1 electron recoils are black.

Figure 3-3

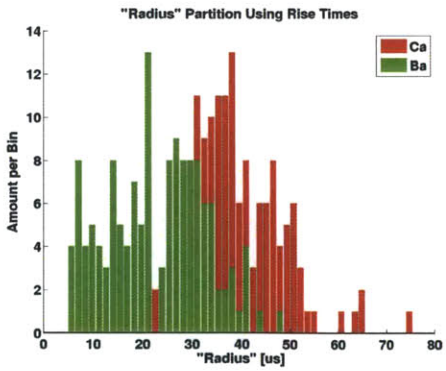

(a) Radius quantity using my MATLAB fitted pulses, energy range apprimately 10-20keV.

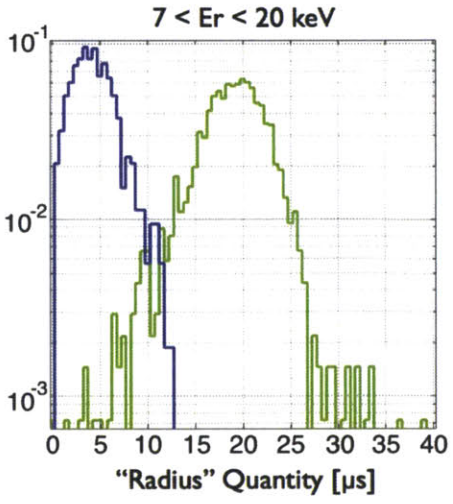

(b) Radius quantity histogram by S. Hertel and M. Pyle. Nuclear recoils are green and electron recoils are blue.

Figure 3-4

Chapter 4

Markov Chain Monte Carlo (MCMC)

4.1 Introduction

If the parameters of the fit are to be used to distinguish event types, then the χ^2 space of the fit function must be thoroughly checked. If, for example, the χ^2 space of a parameter was multi-modal, the fitter wouldn't necessarily converge on the same value each time that pulse type is fit. This parameter would then possibly not be useful for discrimination. To explore the χ^2 space, an analysis called Markov chain Monte Carlo, MCMC, was used.

4.2 MCMC Method Description

The most basic way to determine the shape of the χ^2 function is to perform a grid calculation. This method calculates values of the χ^2 function along a grid of equally spaced points in parameter space. Another method for determining the shape of the χ^2 function is to sample it, or choose values so that the χ^2 function doesn't have to be calculated for large unnecessary regions of the parameter space. The MCMC is an algorithm which greatly increases the efficiency of exploring the χ^2 space of a high parameter function. Since the functional form being used to fit the phonons has 9 free parameters, doing a grid calculation of the χ^2 space would be extremely inefficient. The MCMC algorithm is more efficient because it explores the regions of interest, or

the regions around where the χ^2 is minimized, at a higher density than the regions of high χ^2 values.

4.2.1 Probability Functions

Say there is a function with m parameters, $\vec{\theta} = \{\theta^{(1)}, \theta^{(2)}, ..., \theta^{(m)}\}$. The goal is to find the posterior probability density function (PDF), $P(\vec{\theta}|data)$. The PDF is the probability of a parameter having a certain value given a data set which it describes. In this case, there are 9 parameters that yield a function which can be compared to the phonon pulse. The PDF describes the probability that a set of these 9 parameters is accurate within statistical fluctuation to describe the original phonon pulse.

Bayes Theorem gives us a relation:

$$P(\vec{\theta}|data) = \frac{P(data|\vec{\theta}) \cdot P(\vec{\theta})}{P(data)}, \tag{4.1}$$

where $P(\vec{\theta})$ is the prior probability, which describes the degree of belief in the parameters before observing the data, and $P(data)$ is the probability of the data, where in this case, the data is the phonon pulse. Because $P(data)$ doesn't depend on the parameters, it will be the same in all $P(\vec{\theta}|data)$ functions and is essentially a normalization factor. The function $P(data|\vec{\theta})$ is called the likelihood function, or $\mathscr{L}(\vec{\theta})$. This function describes the probability that the data was observed given a set of parameters. This can be directly calculated as a function of χ^2, so it is helpful in leading us to the posterior PDF which would be harder to calculate directly.

The individual parameter posterior PDFs can then be calculated by marginalizing the multidimensional $P(\vec{\theta}|data)$:

$$P(\theta^{(\alpha)}|data) = \int_{all\beta \neq \alpha} P(\theta^{(\beta)}|data)\, d\theta^{(\beta)}. \tag{4.2}$$

4.2.2 Metropolis-Hastings Algorithm

The Metropolis-Hastings algorithm is the method that the MCMC uses to sample the parameter space in a more efficient way than grid sampling. A Markov chain

is a sequence of N points, $\{\vec{\theta}_i\}_{i=1,...,N} \equiv \{\vec{\theta}_1, \vec{\theta}_2, ..., \vec{\theta}_N\}$ which we obtain using the Metropolis-Hastings algorithm. The algorithm causes the number of samples in a region of parameter space to be proportional to the PDF value in that region. The values of the chain are determined using the following procedure [5]:

1. From each $\vec{\theta}_i$, a new trial point is suggested using a distribution, $q(\vec{\theta}_{trial}|\vec{\theta}_i)$.

2. The probability of the trial value to be accepted as the next value in the chain is:

$$a = \min\Big(1, \frac{\mathscr{L}(\vec{\theta}_{trial}) \cdot q(\vec{\theta}_{trial}|\vec{\theta}_i)}{\mathscr{L}(\vec{\theta}_i) \cdot q(\vec{\theta}_i|\vec{\theta}_{trial})}\Big) \tag{4.3}$$

   If q is a symmetric function (for example a Gaussian), then the q in the numerator and denominator cancel. This equation means that if $\vec{\theta}_{trial}$ is more likely to fit the data than $\vec{\theta}_i$, it will become the next entry in the Markov chain with probability 1. If the trial point is less likely than the previous point in the chain, then it will only become the next value in the Markov chain with a probability proportional to that likelihood ratios, a.

3. If $\vec{\theta}_{trial}$ is accepted, then $\vec{\theta}_{i+1} = \vec{\theta}_{trial}$. Otherwise, $\vec{\theta}_{i+1} = \vec{\theta}_i$.

4. The process is repeated until there are N points in the chain.

For my MCMC, the likelihood function is given as $\mathscr{L}(\vec{\theta}) = exp(-\chi^2/2)$, where χ^2 is calculated between the actual data and the curve produced by the 9 parameters given in $\vec{\theta}$.

There were two trial functions, $q(\vec{\theta}_{trial}|\vec{\theta}_i)$'s, that were used. The first MCMC run, a simple Gaussian was used with a mean of $\vec{\theta}_i$. After the MCMC was finished, 9 histograms of the parameters from the chain were made from the Markov Chain before any quality selections were applied. From these histograms, all entries of the covariance matrix were calculated. This matrix was used to find the mean values for each parameter, as well as the covariance between all of the parameters. Next, the MCMC was run again, but with a multivariate Gaussian trial function instead of a single dimensional Gaussian trial function. This would lead to much more efficient

sampling of the parameter space because better trial values would be suggested, causing more trial $\vec{\theta}$ values to be accepted. The quality selections were then applied to this second chain to yield a statistically independent subset chain.

4.2.3 Markov Chain Quality Selections

The Markov chain is set up in such a way that each element of the chain depends directly on the one preceding it. The goal however, is to get random samples from the PDF, and for samples to be random they must be uncorrelated. Two methods of sub-sampling were used to select a statistically independent subset of the Markov chain to accurately reflect the PDF.

Burn-In Length: The burn in length corresponds to a number of steps to be removed from the beginning of the chain. The purpose of removing these values is to lose the information about the starting point of the chain. The burn in length is estimated by the first step reaching the median value of the target PDF. Therefore, all steps before the first time the median value of the distribution is hit are discarded.

Correlation Length: The correlation length, l, is the length between steps such that they are uncorrelated. To calculate this for each parameter, the autocorrelation function, $c_j^{(\alpha)}$, where j is the distance between steps and α is the parameter, was calculated. For each parameter, the correlation length was chosen by taking the smallest j such that $c_j^{(\alpha)} < 1/2$, where $1/2$ has been shown to be sufficient to yield uncorrelated results [5]. After each correlation length has been found, the maximum one is chosen to be the overall correlation length. Starting with the first step of the chain, every l^{th} step after is taken for the final chain. See Figure 4-1 for an example of the autocorrelation functions for the Markov chains.

4.3 Implementation

In order to run the MCMC, a fake pulse with noise was made to model the data, so that we could test how well the true values of the pulse shape were found while knowing the true values, and so that we could have control over signal to noise ratio,

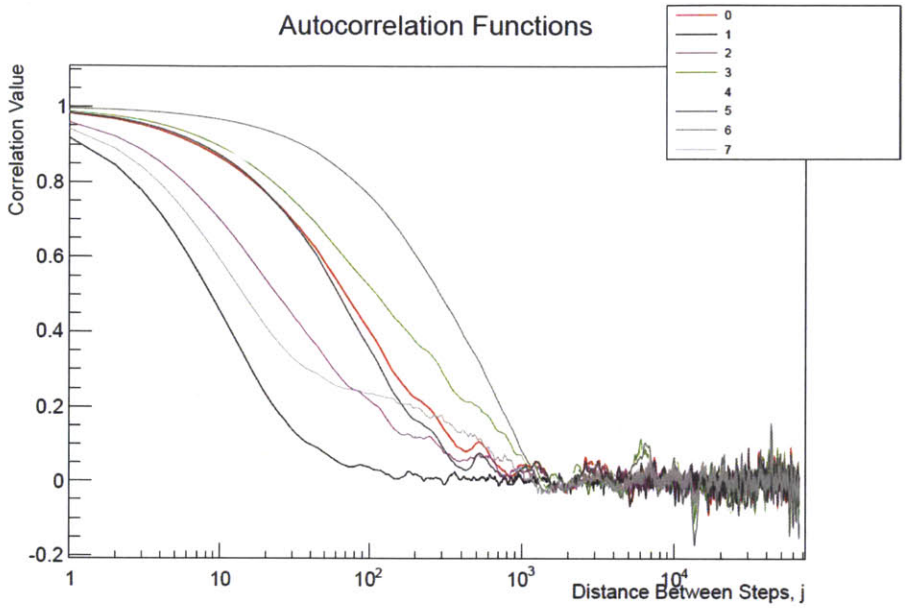

Figure 4-1: The autocorrelation function of each parameter's Markov chain.

and thus mimic different energies. The parameters for the fake pulse were chosen to create a pulse that matched an example real data pulse of approximately 30 keV. Each data point had noise from a Gaussian distribution added to it.

Each parameter was given a range restriction reflecting the restrictions used when fitting. These restrictions were implemented by setting the probability of acceptance for $\vec{\theta}_{trial}$, a, to be 0 when a parameter out of the range was selected.

The MCMC was incredibly inefficient for all 9 parameters (possible reasons why in discussion below), so 8 out of the 9 parameters were used for the MCMC run, R_s being the fixed parameter.

4.4 Checks

There were a variety of checks done on the MCMC. These were both to make sure it was working properly, and to make sure the functional form's χ^2 space was unimodal for a variety of different pulse types. The MCMC output is displayed on the lower triangular half of an 8x8 grid, see Figures 4-5 through 4-11. The 8 plots on the diagonal are histograms of the MCMC results for each parameter. The parameters are

labeled 0-7, corresponding to each parameter in the order $A_f, T_f, R_f, F_f, A_s, T_s, F_s$, and $Shift$. All of the other plots on the grid are 2-D histograms of each combination of the parameters to see how they are correlated. The figures associated with the MCMC checks are all found at the end of the MCMC chapter.

4.4.1 Distribution Widths

The goal of this check was to make sure that the widths of the resulting Gaussian distributions for the parameters matched the expected widths when looking at the reduced χ^2. The MCMC was run on just the F_f and R_s parameters, while keeping the other 7 parameters fixed. Separately in MATLAB, a grid calculation of the reduced χ^2 values for a range of F_f and R_s values.

The results can be seen in Figure 4-2. These two methods were expected to produce very similar plots because they are both probing the χ^2 distribution of the same pulse. They won't be exact however, because the pulse noise realization was different in both cases. The results from the MCMC are very similar to the results when comparing the χ^2 values by hand in MATLAB, confirming the MCMC was accurately calculating the likelihood function.

4.4.2 Different Pulse Shapes

The MCMC was tested on an alternative pulse shape to confirm that it worked for a variety of pulse types. The pulse shaped used for all of the checks, as well as the alternative one used for this check, can be seen in Figure 4-3. The MCMC results, seen in Figure 4-4, look consistent with the original pulse used.

4.4.3 Variable Range

The MCMC was first run using relatively tight ranges for each parameter. The result, see Figure 4-5, showed that some of the parameters were railing against these bounds. This means that potentially, the true χ^2 minimum was outside of the ranges initially set for the parameters.

These ranges were widened until no railing was visible, the results in Figure 4-6. The only exception to this widening was restricting the second time shift, T_s, to be greater than 0, even though there is some slight railing at 0. This is because the slow pulse by definition was to come after the first pulse, and if the time were negative, the pulses had the chance of switching.

These widened ranges reflect the ranges that were inputted when fitting the pulse during the analysis, see Table 3.1 for a list of these values.

4.4.4 Different Noise Levels

Because the hope that the time-domain fitting analysis method would be useful at low energies, it was necessary to use the MCMC to check the parameter PDFs at a variety of low energies. The ratio of the noise to the amplitude can be used to find what the energy would be of events represented by the fake pulses generated. The effective energy of the pulse used for all of the other checks was 30keV. The effective energies that were further looked into in this check were 10keV down to 2keV in increments of 2keV. These results can be found in Figures 4-7, 4-8, 4-9, 4-10, and 4-11.

These results show that all of the parameters continue to be uni-modal even down to as low as 2keV in energy.

4.4.5 Four Parameters Only

As is described in detail in the following chapter, section 5.1, speed performance is an important factor when implementing the time-domain fitting. To speed up the processing, only 4 parameters were used when fitting: A_f, R_f, F_f and A_s. The MCMC was run with just these four parameters on the same 30 keV pulse used for the other checks, and the results were very nice Gaussian distributions centered around the correct parameter values, see Figure 4-12.

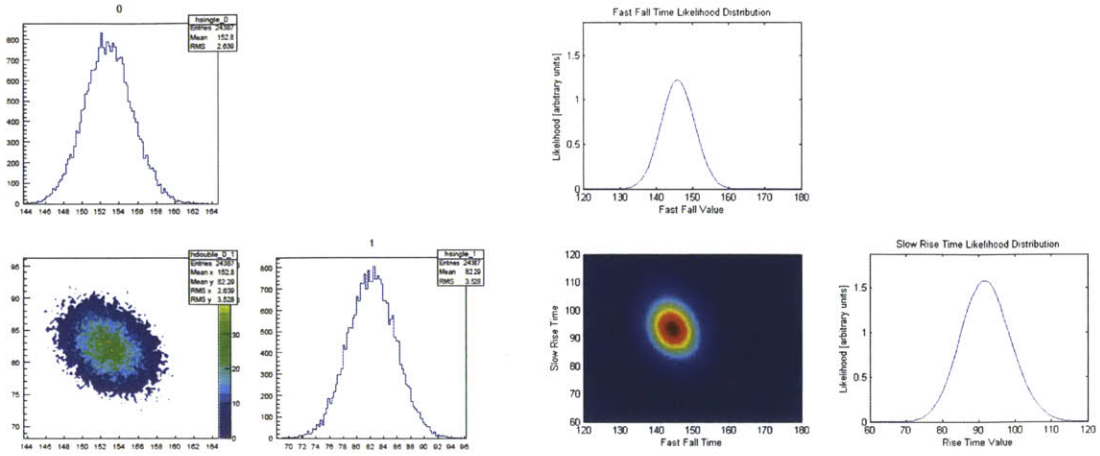

Figure 4-2: MCMC comparison to MATLAB grid calculation of χ^2 space with two variables, R_s and F_f.

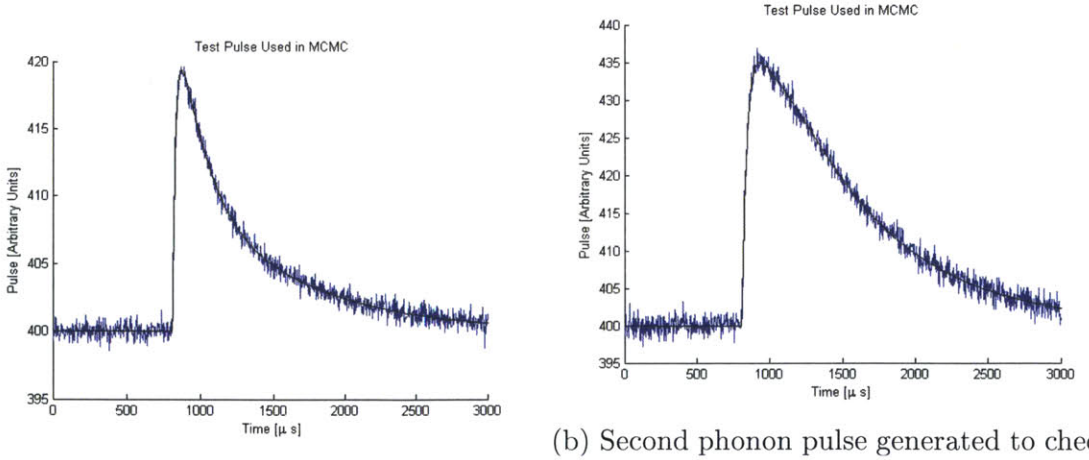

(a) Phonon pulse generated for MCMC use.

(b) Second phonon pulse generated to check the MCMC was working properly for more than one pulse shape.

Figure 4-3

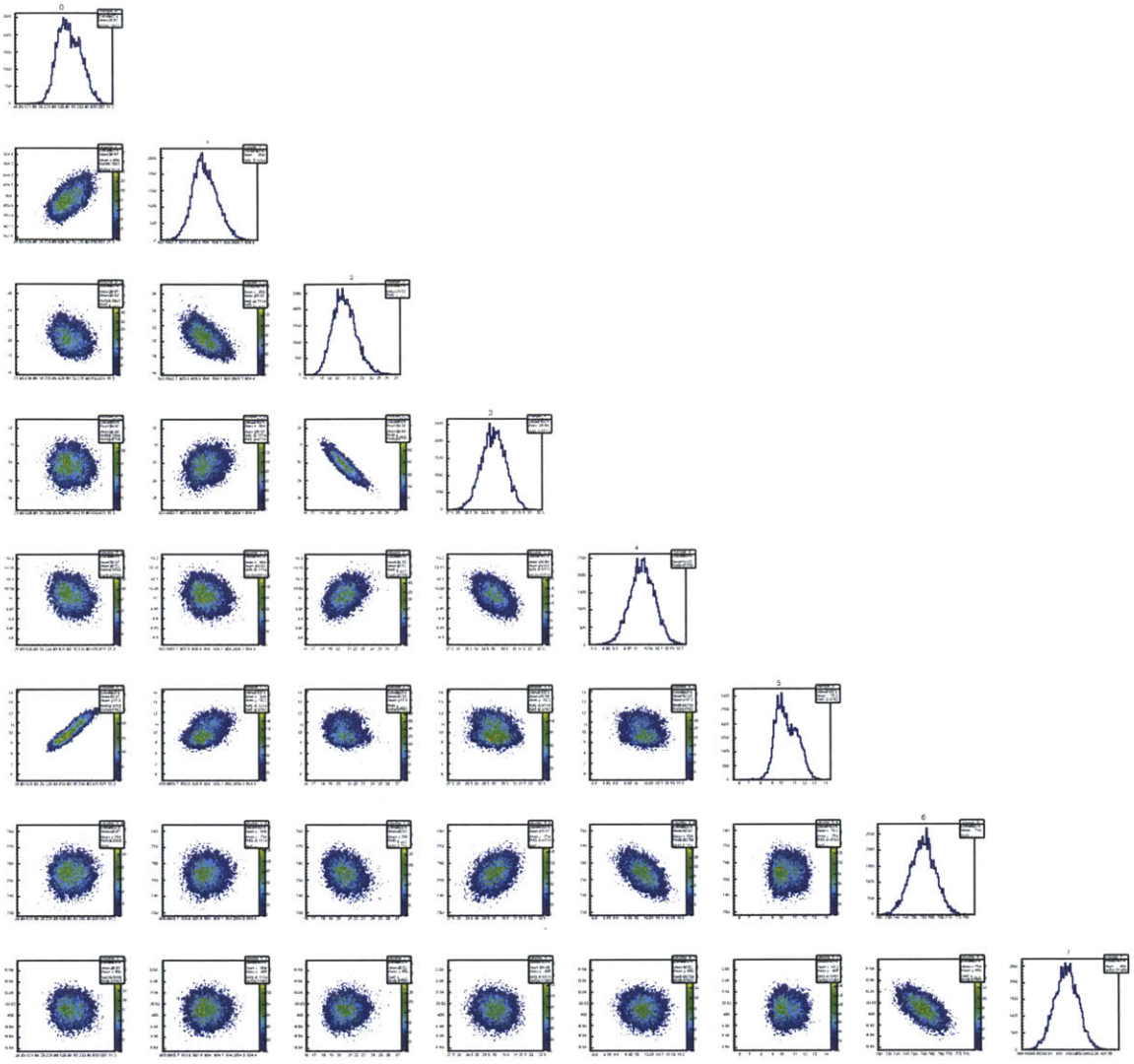

Figure 4-4: MCMC histogram using the alternative pulse shape. Parameter order: $A_f, T_f, R_f, F_f, A_s, T_s, F_s$, and $Shift$.

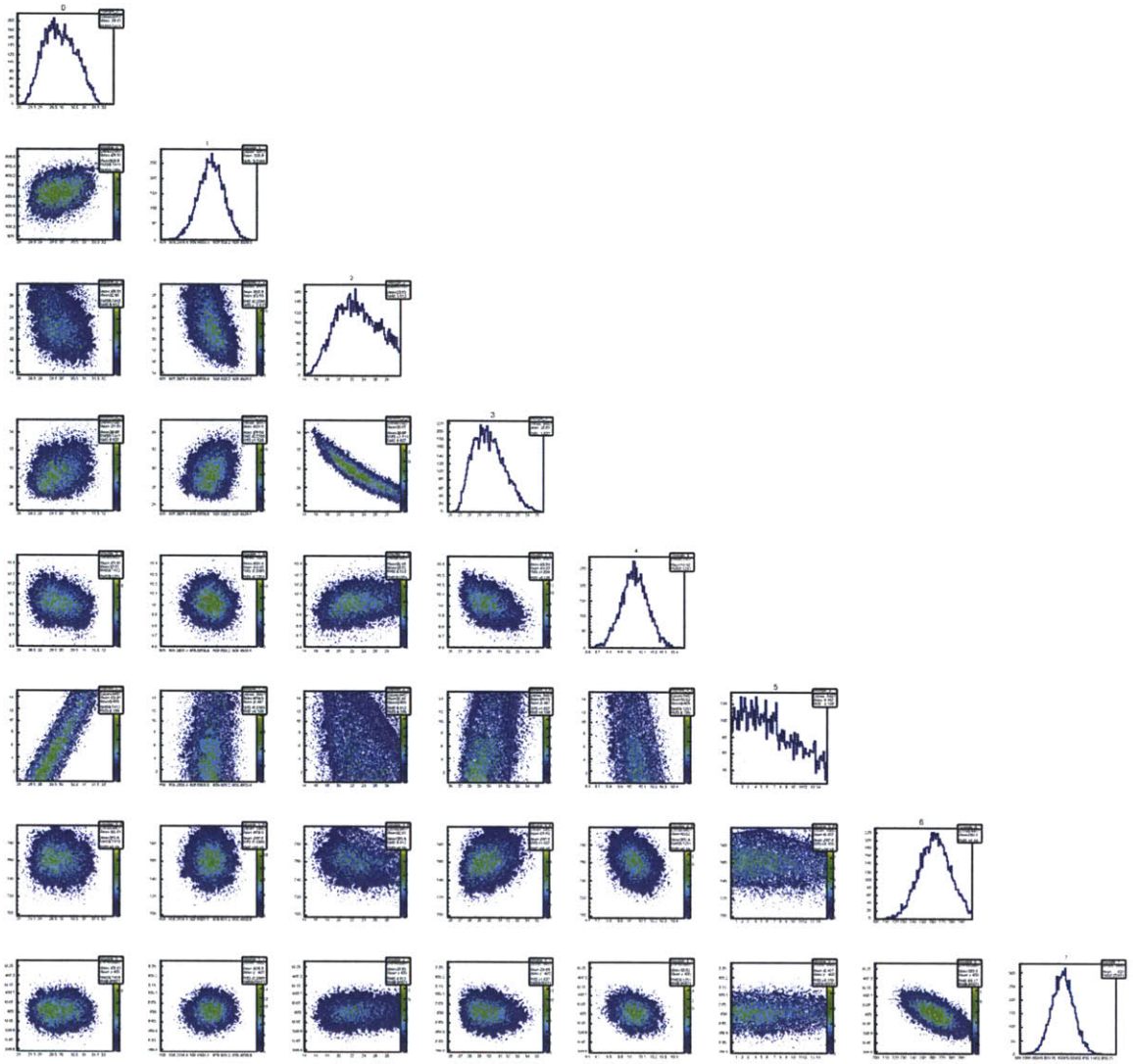

Figure 4-5: MCMC histogram with restricted parameter ranges. Parameter order: $A_f, T_f, R_f, F_f, A_s, T_s, F_s$, and $Shift$.

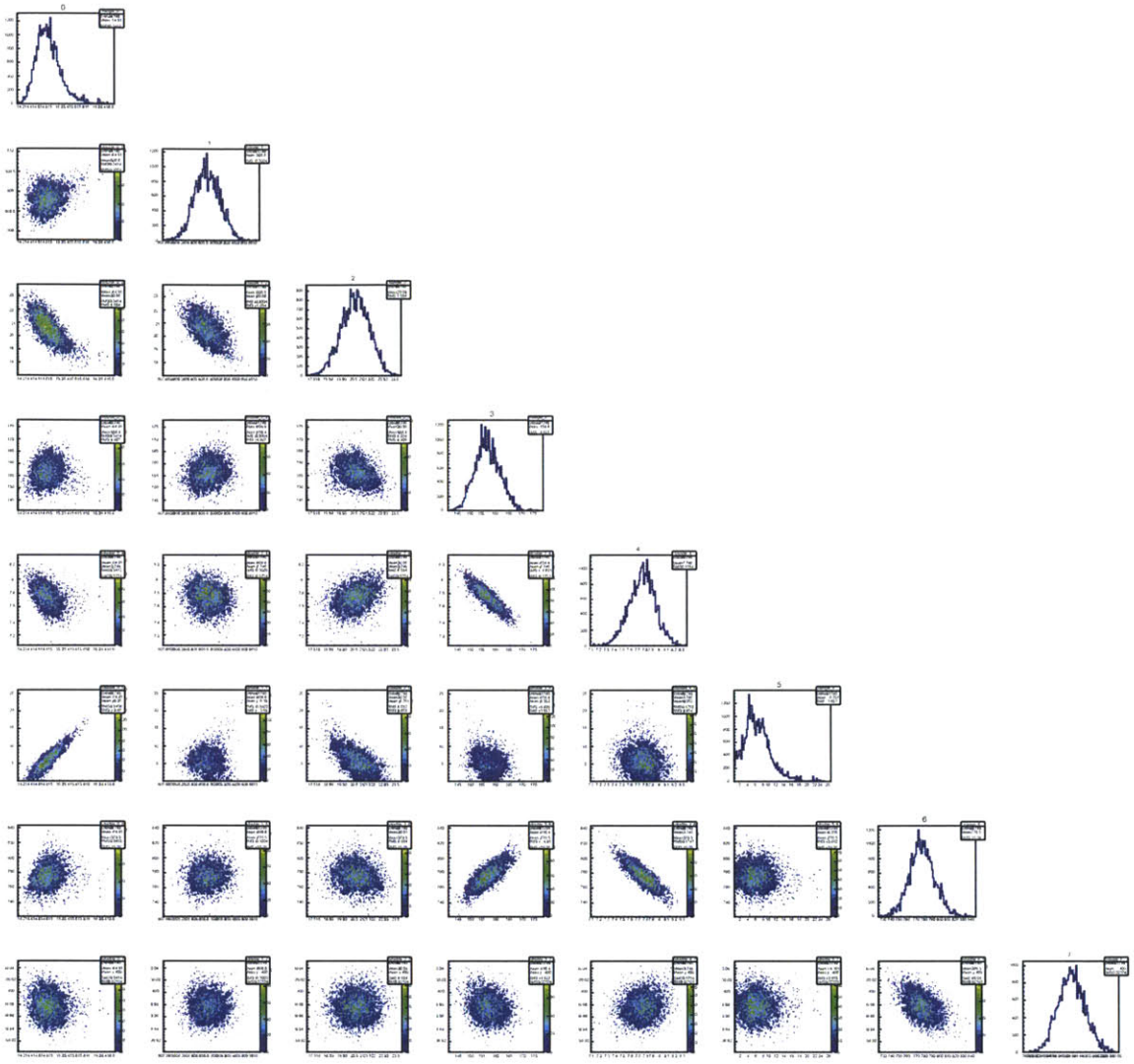

Figure 4-6: MCMC histogram with very wide parameter ranges, with the exception of keeping T_s greater than 0. The effective energy of this pulse is 30keV. The allowed parameter ranges in this run were the ones that were then used in the implementation of fitting the pulse to the functional form. Parameter order: $A_f, T_f, R_f, F_f, A_s, T_s, F_s$, and $Shift$.

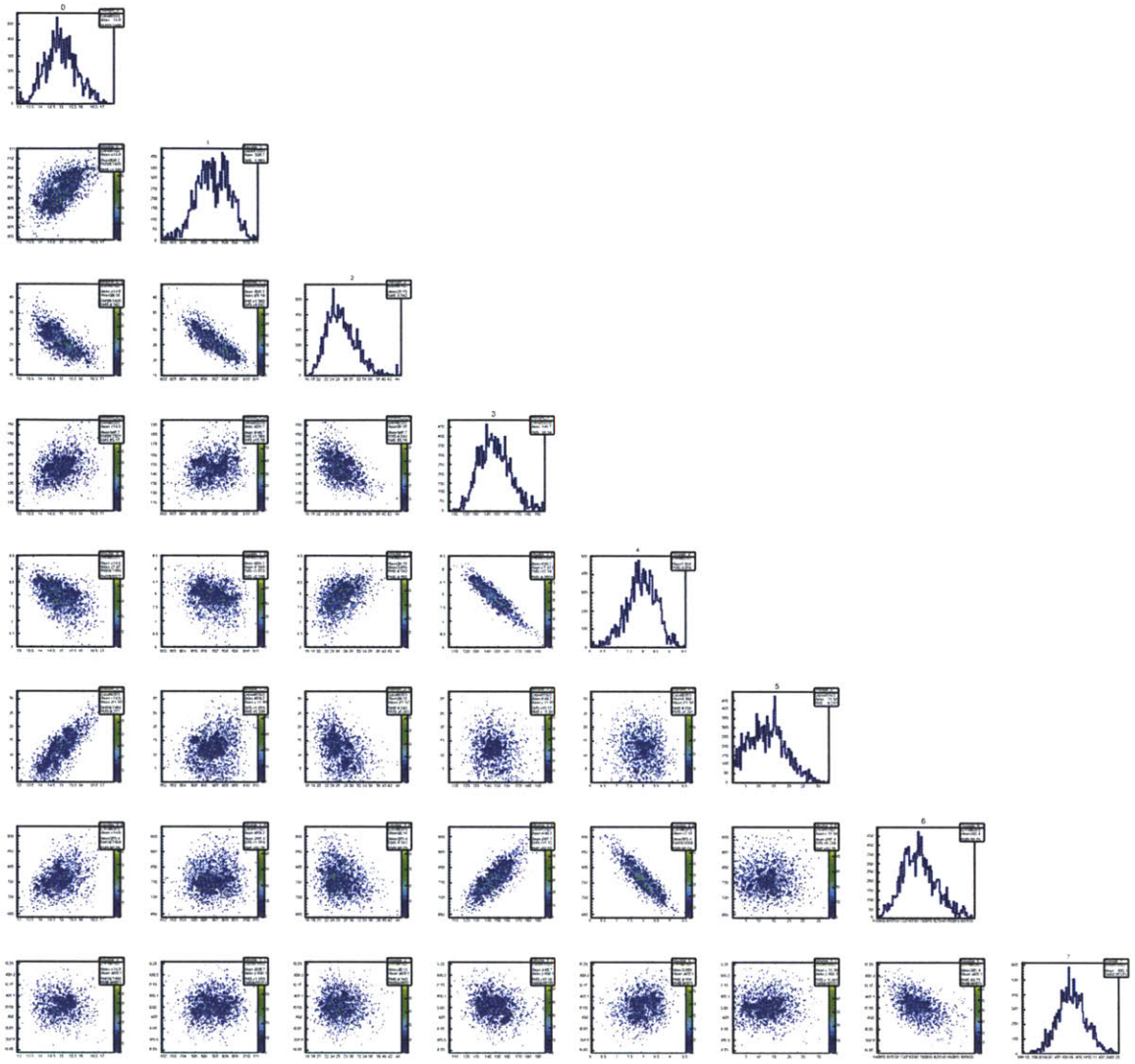

Figure 4-7: MCMC histogram with an effective energy of 10keV. Parameter order: $A_f, T_f, R_f, F_f, A_s, T_s, F_s$, and $Shift$.

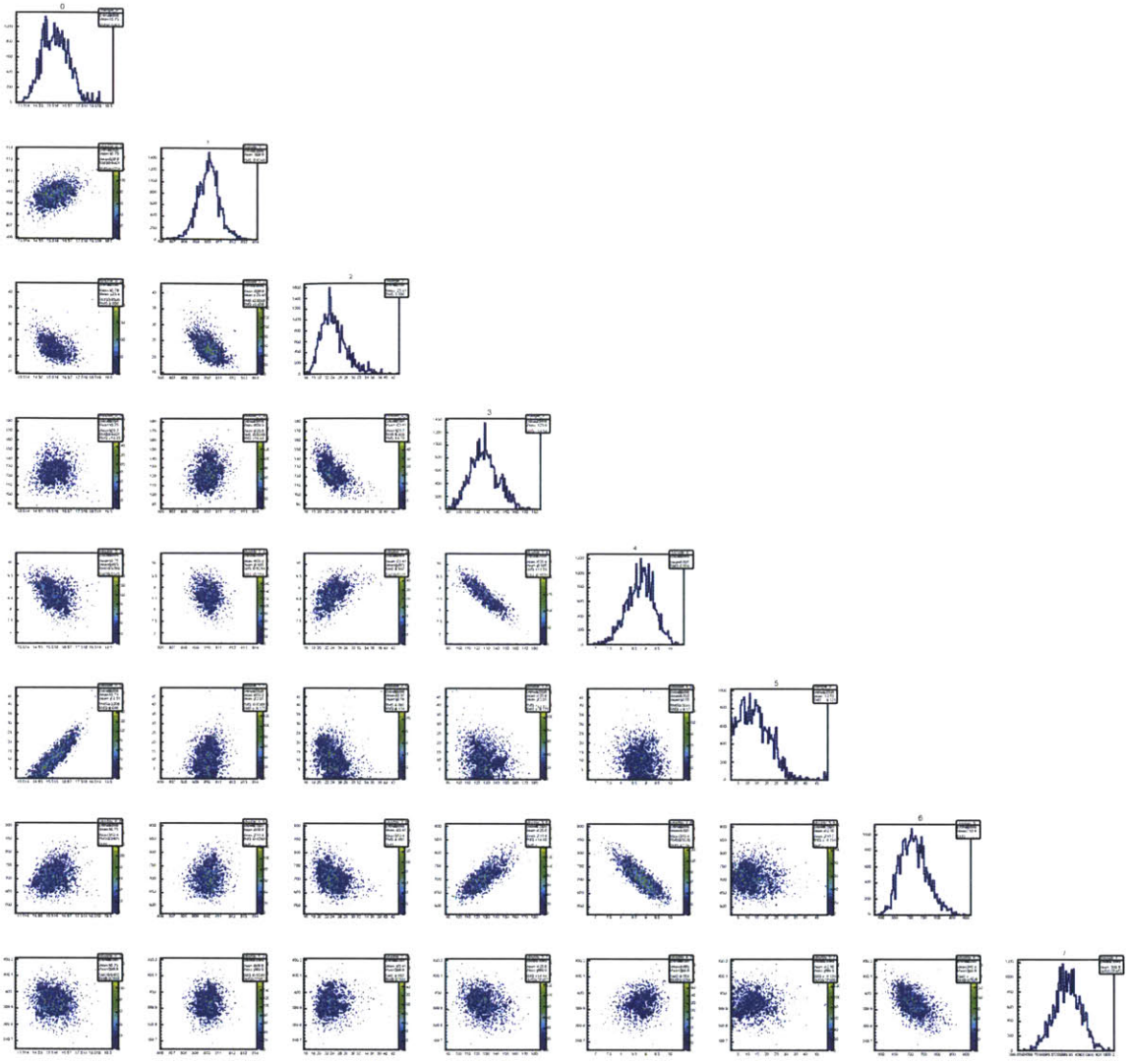

Figure 4-8: MCMC histogram with an effective energy of 8keV. Parameter order: $A_f, T_f, R_f, F_f, A_s, T_s, F_s$, and $Shift$.

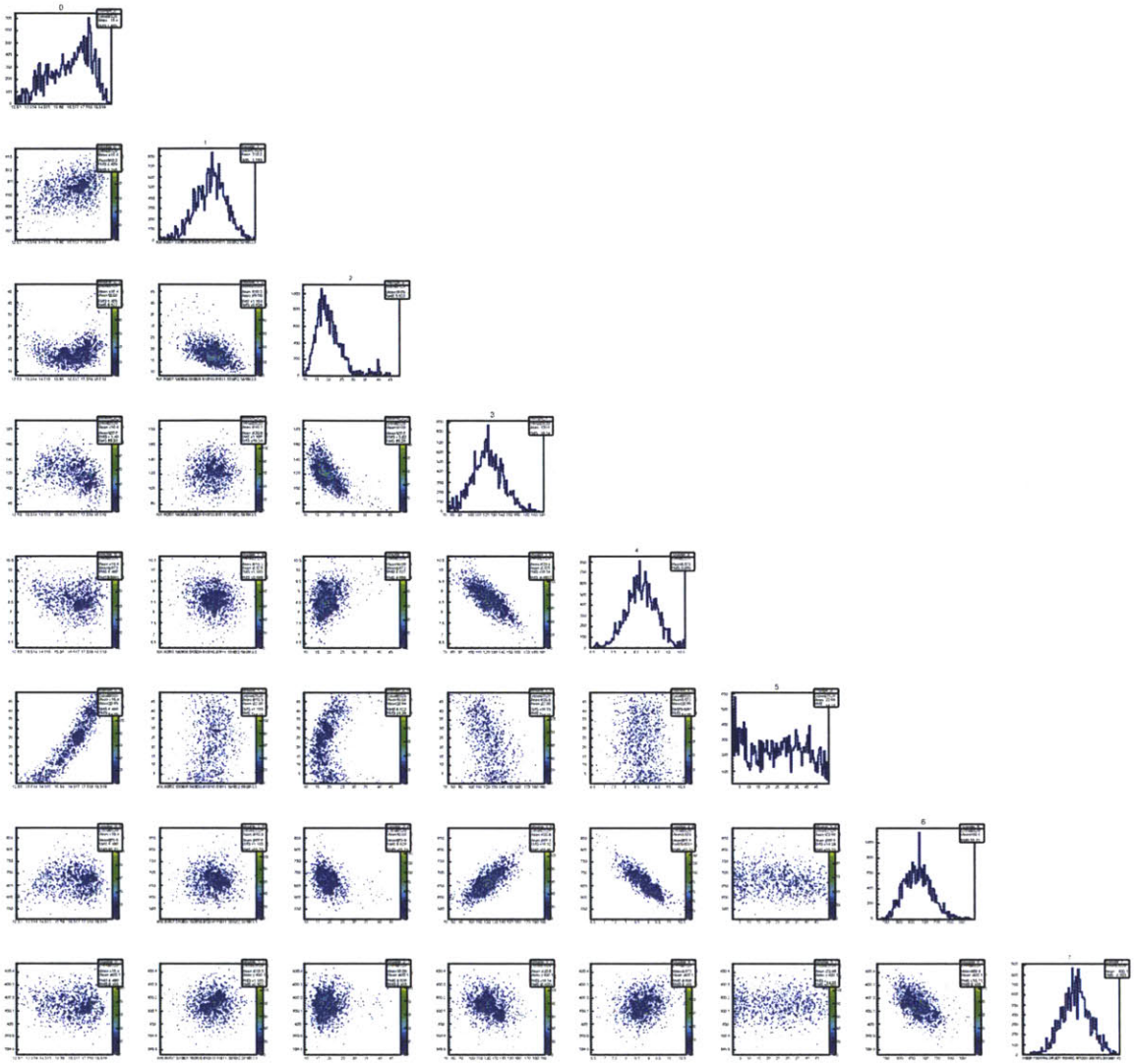

Figure 4-9: MCMC histogram with an effective energy of 6keV. Parameter order: $A_f, T_f, R_f, F_f, A_s, T_s, F_s$, and $Shift$.

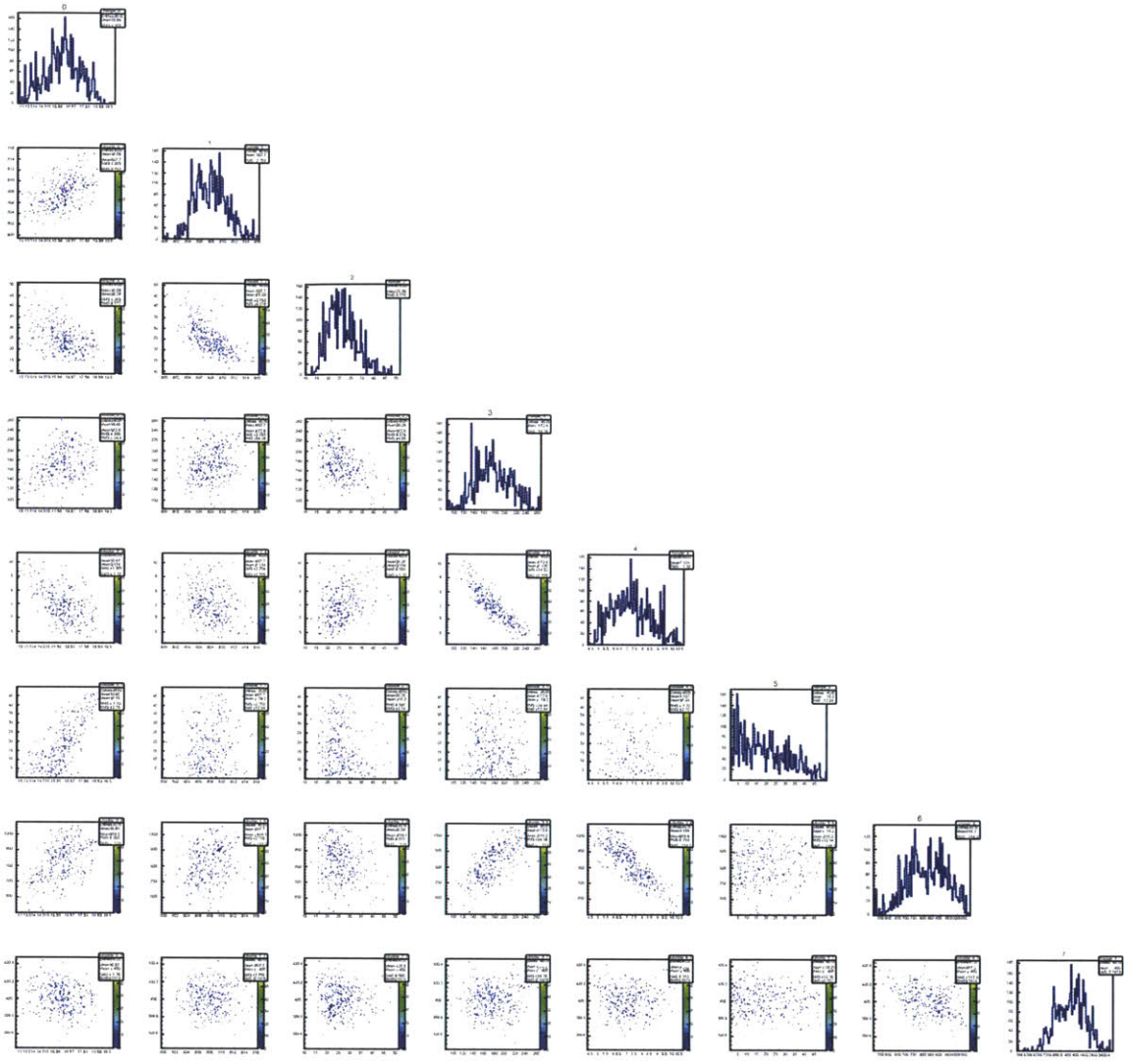

Figure 4-10: MCMC histogram with an effective energy of 4keV. Parameter order: $A_f, T_f, R_f, F_f, A_s, T_s, F_s$, and $Shift$.

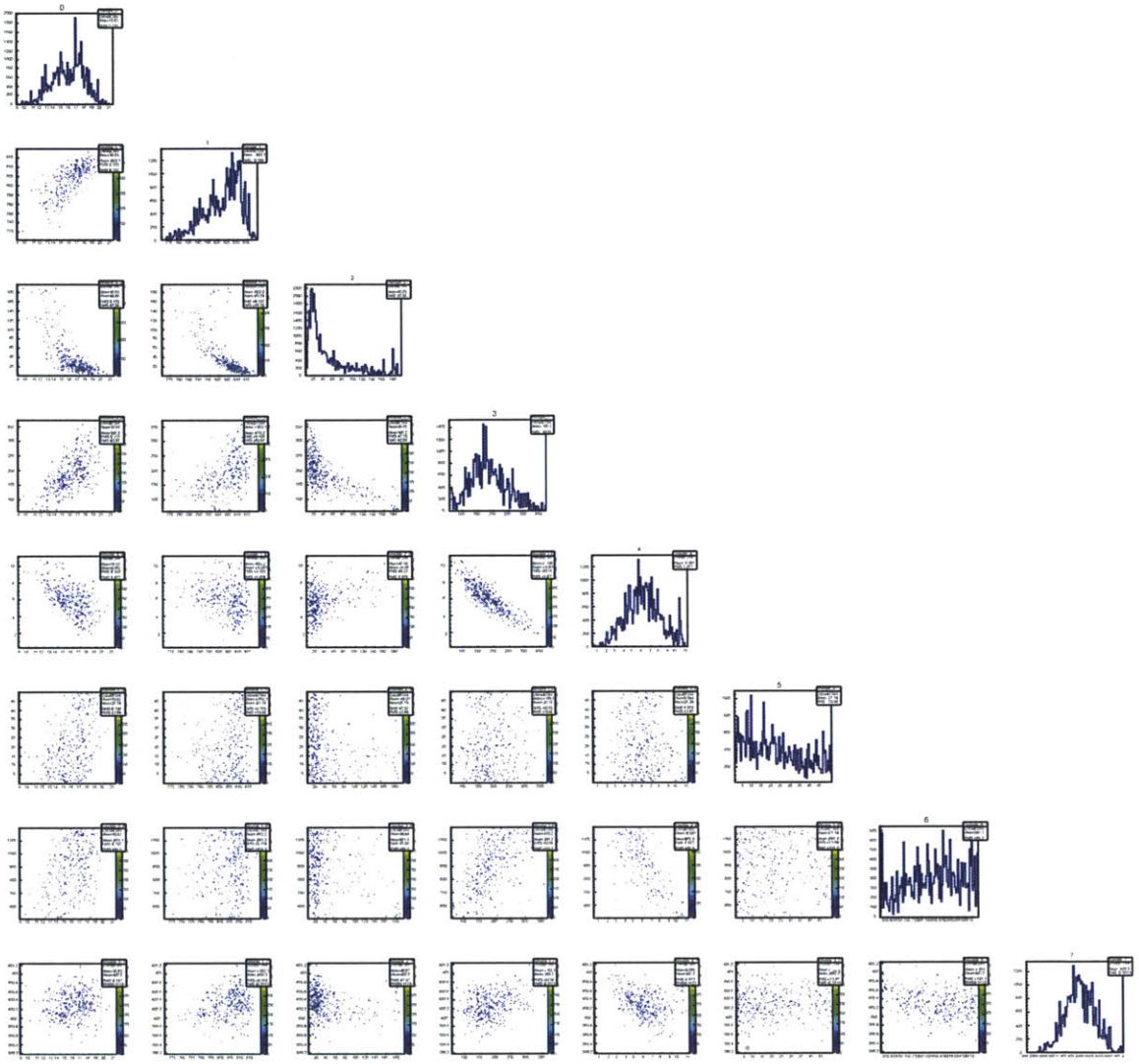

Figure 4-11: MCMC histogram with an effective energy of 2keV. Parameter order: $A_f, T_f, R_f, F_f, A_s, T_s, F_s$, and $Shift$.

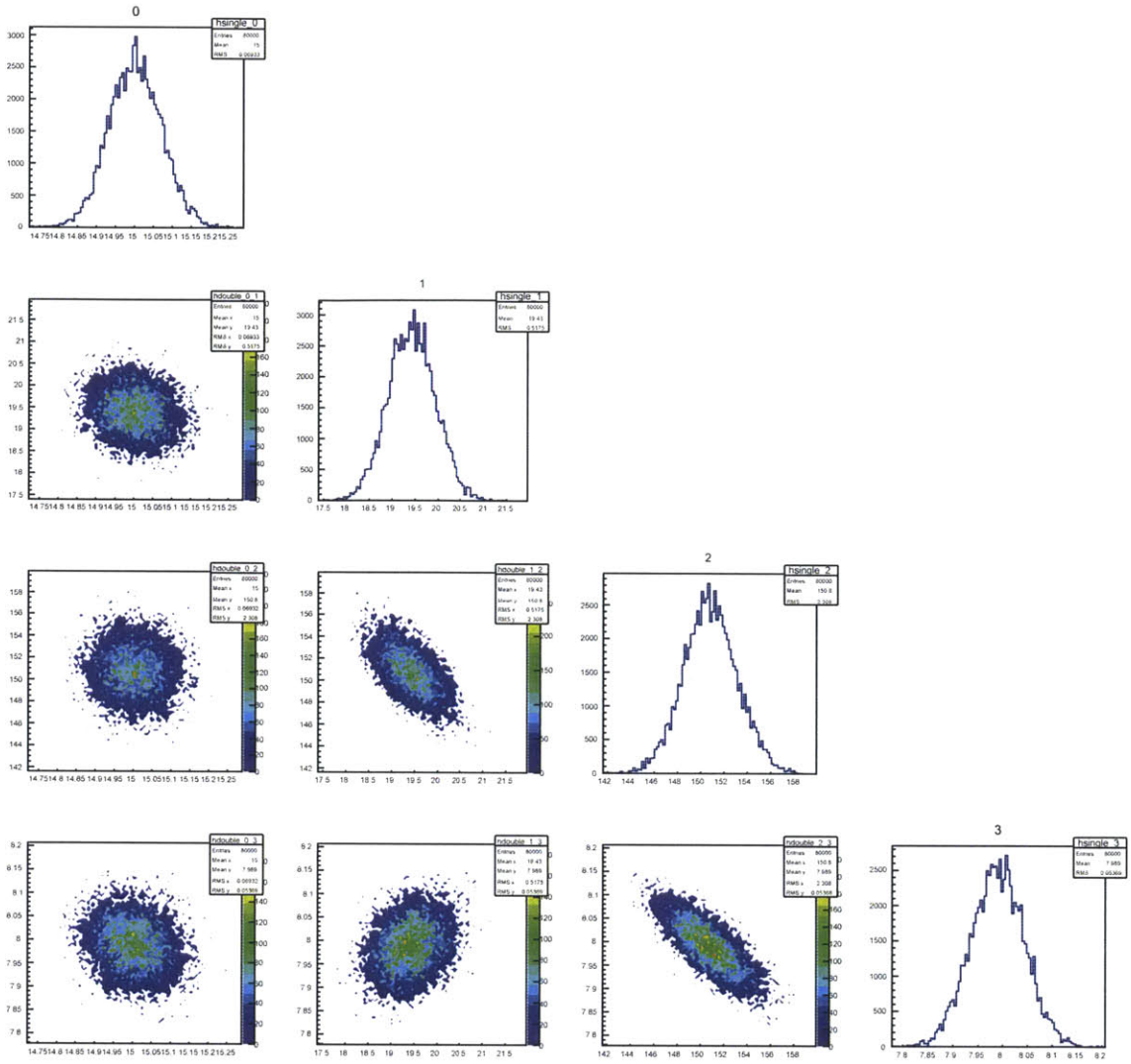

Figure 4-12: MCMC histogram with the final 4 parameters used when implementing the time-domain fitting. The order of the parameters in the figure are: A_f, R_f, F_f and A_s.

Chapter 5

Implementation and Analysis

5.1 Implementation into CDMS BatRoot

BatRoot is an analysis package which CDMS uses to convert raw data from the detectors to reduced quantities, RQs. These RQs include quantities such as event energy, event number, maximum pulse height, etc. The pulse fitting algorithm was implemented into CDMS BatRoot yielding a set of RQs including all of the fit parameters and the χ^2s of the fits, for each side of the detector.

5.1.1 Speed

An important factor when considering the potential usefulness for this analysis method is the speed at which it performs compared to the current analysis algorithms, and how much it would slow down data production. A variety of combinations of floating parameters for the time-domain fitting algorithm were tested for time against the current standard algorithms, see Table 5.1. There were 500 events processed on a single core of a Fermilab computer. These quick tests showed that adding one parameter over the initial 4 increased processing time significantly. In order to keep efficiency high, we decided to do all initial processing, testing, and discrimination analysis with just these 4 floating parameters. The five parameters not used during this implementation were chosen because they could either be estimated via current

CDMS algorithms, they could be estimated directly from the pulse shape without fitting, or they did not have a large impact on the quality of the fit.

	ptNF	4 par	4 par+T_f	4 par+R_s	4 par+F_s
Time above baseline (min:sec)	4:46	4:31	6:36	6:46	6:41

Table 5.1: Time above the baseline data production speed for the time-domain fitting processing with different floating parameters. The 4 parameters used in all runs were A_f, A_s, F_f, and R_f. ptNF is the total phonon pulse energy of the event.

Here is a summary of each parameter and how it was implemented:

- A_f and A_s: Floating - Initial: Maximum of trace /2. Range: 0 to 1 (Expected range: 0 to 10^{-7}).
- T_f and T_s: Fixed to the OFdelay RQ from ptOF.
- R_f: Floating - Initial: 100 bins. Range: 10 to 150 bins.
- R_s: Fixed to 150 bins.
- F_f: Floating - Initial: 200 bins. Range: 50 to 200 bins.
- F_s: Fixed to falltime RQ from SingleExponentialFit algorithm.
- $Shift$: Fixed to mean of the first 400 bins.

SingleExponentialFit is an algorithm currently used to fit the tail of each pulse, and OFdelay is an RQ which estimates the start of the pulse.

An additional change that was made to speed up the data processing was only calculating the χ^2 of each pulse between bins 400 and 1400. This should have a minimal effect on the fitting quality because bins 0-400 are just pre-trigger noise, and the bins after 1400 are the tail of the exponential which has already been fit for in SingleExponentialFit, and is the same for every event.

5.1.2 Data

Three data sets from 2 detectors in CDMS's Run 133 were reprocessed using the time-domain fitting algorithm. The first set was ^{252}Cf calibration data, which provides nuclear recoil events from 1-2 MeV neutrons. The second was ^{133}Ba calibration data, which provides electron recoils from several gamma lines between 300 and 400 keV. The third was low-background data, which contains events from a ^{210}Pb surface event calibration source. The lead decay chain can be seen in Figure 5-1.

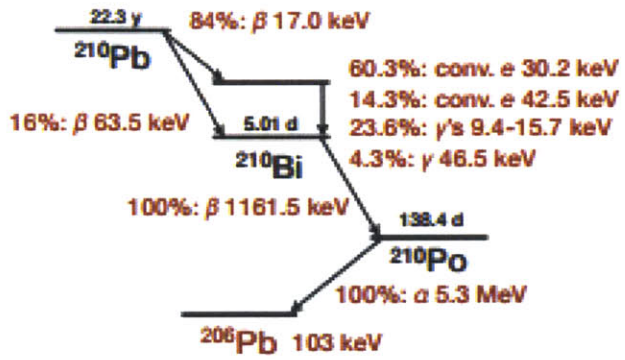

Figure 5-1: The lead decay chain. Lead is used as a calibration for surface events in the low background data set.

5.1.3 Results

Three raw phonon pulses of energies 2.4, 7.8, and 50.4 keV are shown in Figure 5-2. Even with just 4 out of the original 9 parameters of the function used in this implementation, the fits are of high quality, even down to very low energy events.

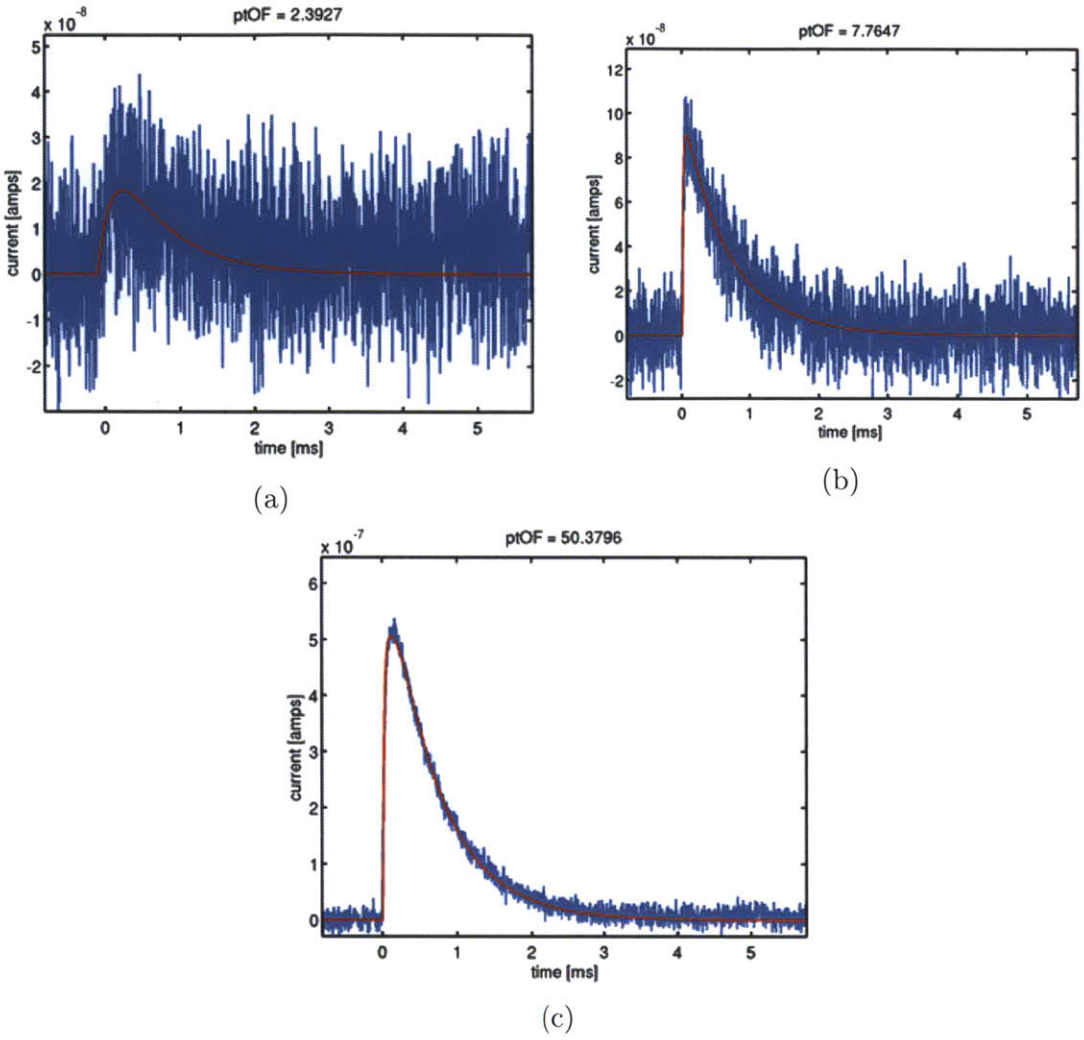

Figure 5-2: Three raw phonon pulses of varying energy from CDMS with fits overlayed in red.

5.2 Boosted Decision Trees Analysis

5.2.1 Boosted Decision Tree Description

Once all the data had been processed, the fit function parameters needed to be analyzed to determine how they could be used in data discrimination.

Decision trees are a machine learning technique which can be used to split data into categories, for example signal and background, or electron and nuclear recoil. The basic idea of a decision tree is using a variety of characteristics of the data to

efficiently classify events when only using one or two of the characteristics might not be enough to distinguish the categories well [7].

The tree is first trained on half of a data set where the type, signal or background, is already known. It is then tested on the other half of the data set to determine efficiency and test for possible over or under training. Once well trained, the tree can be applied to an unknown data set to distinguish between signal and background given the characteristics used during the training.

The training data starts in one node of the tree, the root node. A variety of characteristics of the data are chosen to be used as classifiers. All events are sorted separately using each of these variables. For each sorted list, the best splitting value is determined. This is the value of the variable which best separates the data into signal and background. The cut which most efficiently separates the data is applied, and the node is split into two nodes, one with the mostly signal events, and one with the mostly background events. Each of these nodes then undergoes the same procedure, further splitting the data. This continues until a predetermined criteria is reached, for example a minimum number of events in a node. These final nodes are the end of the tree branches, and are called leaves.

The purity of leaves can be characterized by their "purity value", $p = \frac{s}{s+b}$, where s is the number of training signal events, and b is the number of training background events. A leaf can either be assigned this value, or it can be assigned a binary value representing whether it is mostly signal or background. For example, if the $p > .5$, it could be assigned a value of 1 for signal, and if $p < .5$, it could be assigned a 0 for background.

Some examples of criteria that could be applied to a tree to determine when a node becomes a leaf include:

- Maximum tree depth: When this maximum number of nodes is reached on a tree branch.
- Minimum leaf size: When a node is made with this minimum number of events.
- Perfect separation: If the node has a purity of 0 or 1.

- Failed splitting improvement: If there is no cut on any of the variables which improves the purity of events.

Some variables are not very good at discriminating between categories of data, but do have classification power. These are called weak classifiers. Boosting is a method that combines weak classifiers into a new stable classifier with better discrimination power.

The boosting algorithm creates many trees, linearly combines them with weights, and yields a single variable:

$$BDT = \sum_{k=1}^{N_{trees}} \alpha_k T_k$$

where α_k is the weight given to each training sample, T_k. Each tree is obtained by taking the misclassified events from the previous tree, and giving them more weight when applying cuts. A misclassified event is an event that ends up in a leaf of the wrong type, for example a background event in a signal leaf with purity $p = .8$. The large advantage of this method is that it takes the multidimensional space of many parameters and yields one discriminating parameter. The boosting algorithm also significantly increases discrimination power because of the increased weight for misclassified events.

The Boosted Decision Tree algorithm was applied to the results of the time domain phonon pulse fit.

5.2.2 Results

The BDT output value ranges from -1 to 1, where -1 corresponds to background and 1 corresponds to signal. Each event is assigned a number based on if it is more likely to be background or signal. The results can be seen in Figure 5-3. This is an example histogram from a BDT run of californium data and low-background data in the energy range 30-70keV.

A BDT value chosen as a cut will yield a data set with a specific background rejection and signal efficiency. For example in this plot, if the BDT cut was chosen to

be about -.1, we would have rejected of about 90% of the background while accepting about 90% of the signal.

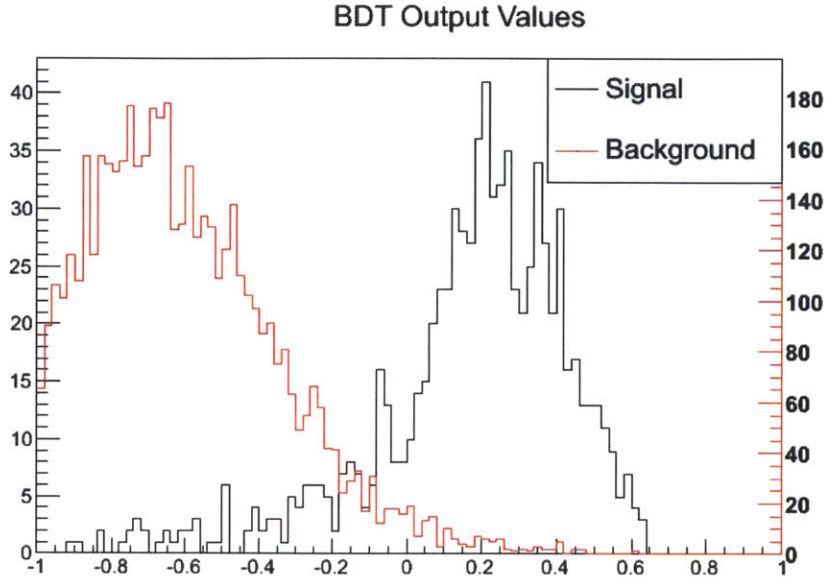

Figure 5-3: BDT run results for 30-70keV low-background and californium events.

Some BDTs were run to test cut efficiency over a variety of energy ranges, for both californium versus barium data (nuclear recoil versus electron recoil), and californium versus low-background data. The results can be seen in Figures 5-4 and 5-6. These plots show the background rejection versus signal acceptance for a variety of BDT cuts between -1 and 1. If the background and signal BDT distributions were exactly on top of one another, then the rejection and acceptance would follow a straight line, as show by the dotted line in the figures. This means that the farther away the curve is from the dotted straight line, the better the discrimination power of the BDT cut.

The BDTs were also run comparing the same data using three partition quantities that CDMS currently uses for discrimination, in order to compare their discrimination power with that of the time-domain fitting parameters. The three quantities used were energy (ptNF), the approximate event radial position (prpartOF) and the approximate event Z position (pzpartOF), all based on the relative amplitude of the signal measured in different phonon channels. The results of those BDT runs can be seen in Figures 5-5 and 5-7.

The time-domain fitting parameter BDT results are farther away from the dotted

line in both cases, meaning they have a stronger discrimination power compared to the quantities currently used in the CDMS algorithms. The difference in the barium versus californium cases are is quite extreme, which is to be expected. This is because the time-domain fitting parameters have much more information about the charge than the three phonon partition variables. For example, an increase in charge causes an increase in Luke phonons, which changes the rise time of the pulse. Barium emits gamma particles, and californium emits neutrons, so this charge information gives a lot of information when discriminating. The ionization information resolution at low energies is poor, so this analysis using only phonons will be able to distinguish events at lower energies.

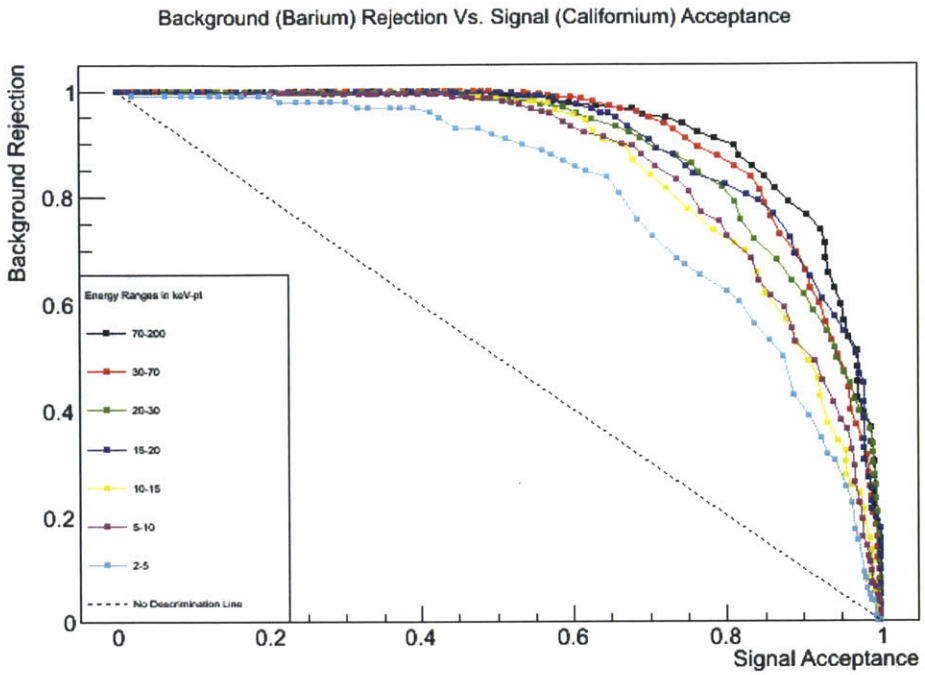

Figure 5-4: Signal acceptance versus background rejection over a variety of energy ranges for *californium versus barium data* for BDTs using time-domain fitting parameters.

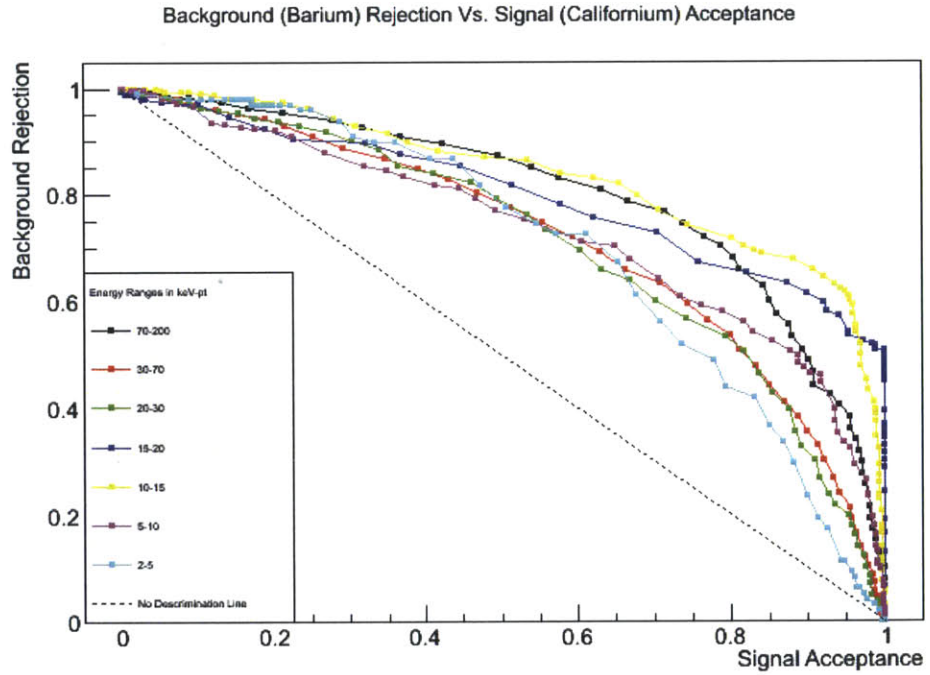

Figure 5-5: Signal acceptance versus background rejection over a variety of energy ranges for *californium versus barium data* for BDTs using 3 partition parameters.

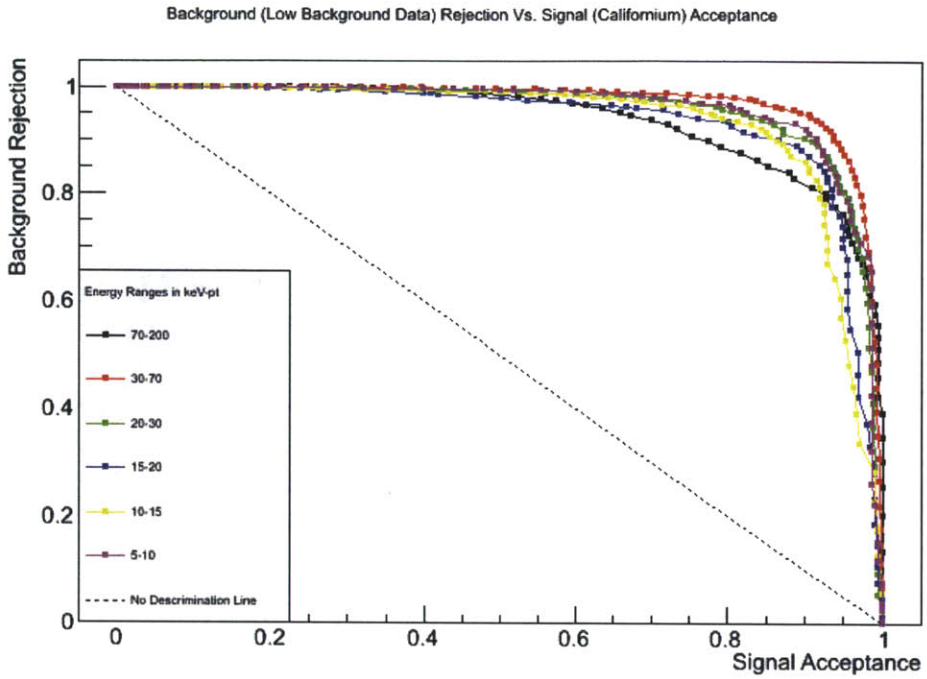

Figure 5-6: Signal acceptance versus background rejection over a variety of energy ranges for *californium versus low-background data* for BDTs using time-domain fitting parameters.

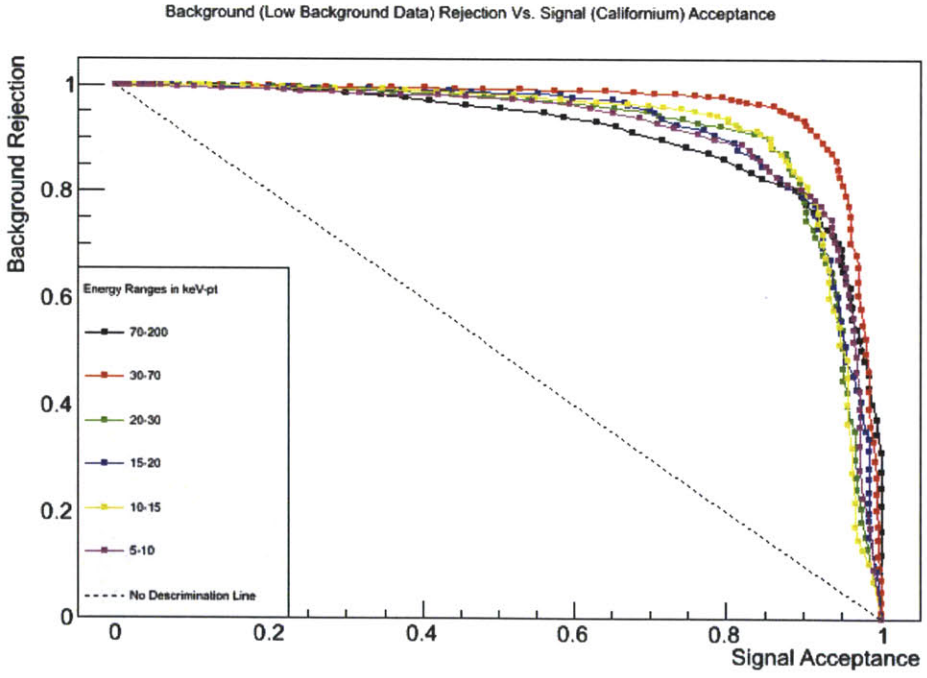

Figure 5-7: Signal acceptance versus background rejection over a variety of energy ranges for *californium versus low-background data* for BDTs using 3 partition parameters.

5.3 WIMP Discrimination

The real interest in this analysis method is the discrimination between WIMP candidates and background events. In order to run the BDT on these two data types, the californium data was weighted to match the expected distribution for a 15 GeV WIMP. Figure 5-8 shows the original energy distribution of the californium data between 5 and 30 keV, along with the newly weighted distribution to match one of a 15 GeV WIMP.

The results of this BDT can be seen in Figure 5-9. Once again, the time-domain fitting parameters gave a much better signal to background discrimination. At a background rejection of 99.4%, the partition parameters had a signal acceptance of 41.1%, while the time-domain fitting BDT had a signal acceptance of 55.1%, a 34% efficiency improvement. These are initial results that will surely get better with optimizing the data selection and BDT.

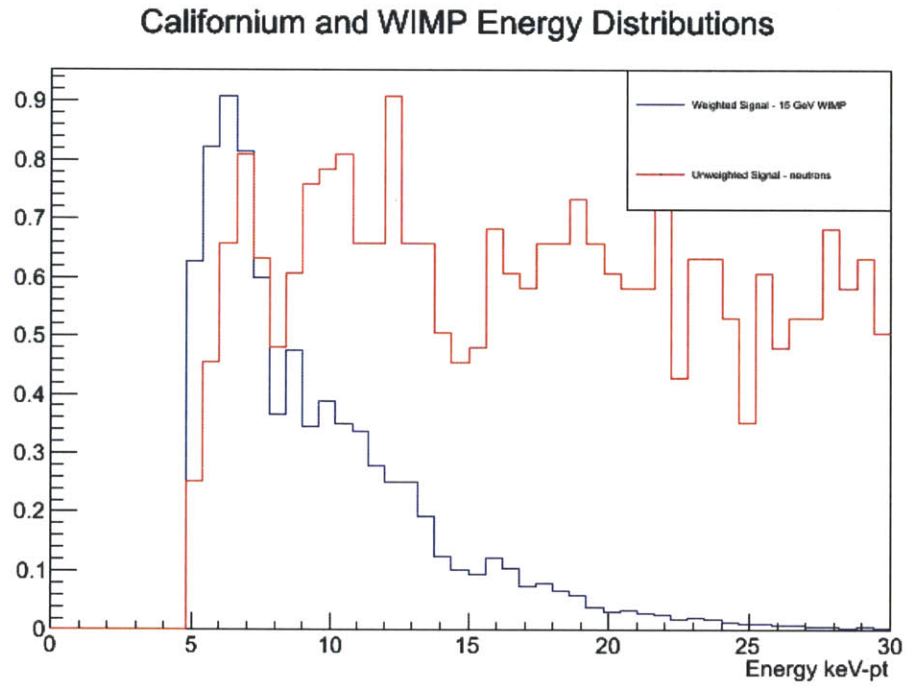

Figure 5-8: The original energy distribution of the californium data between 5 and 30 keV and the newly weighted distribution which matches one of a 15 GeV WIMP.

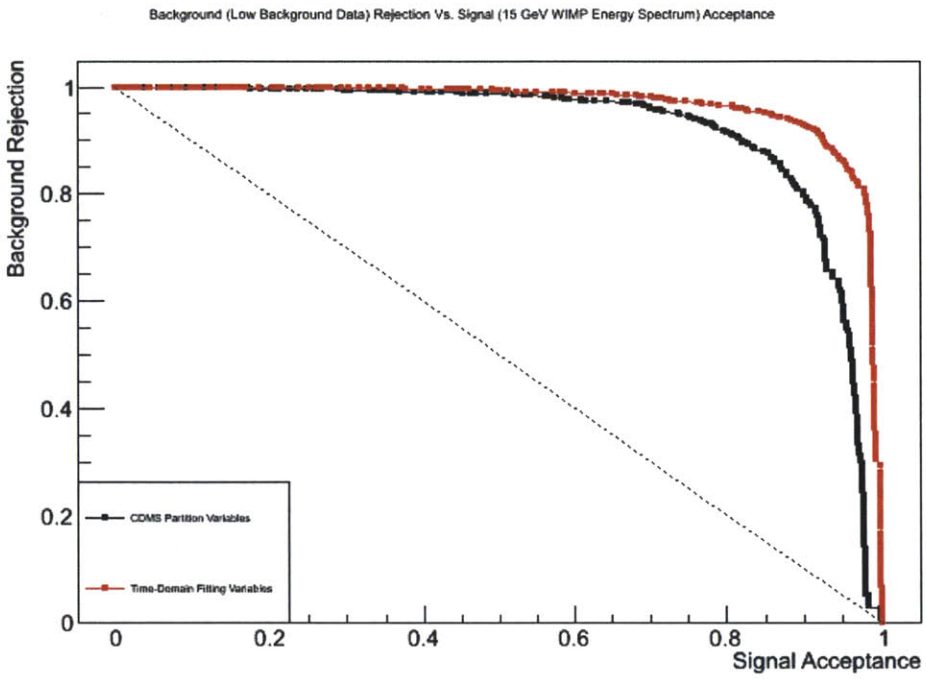

Figure 5-9: Signal acceptance versus background rejection for low background data against a 15 GeV WIMP distribution, using both the time-domain fitting parameters and the partition parameters.

5.4 Conclusion

This first attempt at combining this time-domain fitting algorithm with a Boosted Decision Tree algorithm produced very encouraging results for their potential discrimination power, and there is still a great deal of fine tuning which can be done in order to further improve the experiment's sensitivity to dark matter.

The BDT could be optimized in many ways. The quantities chosen for the BDT were simply the fit parameters, but other quantities such as the rise time discussed in section 3.2, could further improve the discrimination. Also, the BDT itself has many parameters, such as minimum leaf size discussed in section 5.2.1, which could be optimized.

There are a large number of studies which could be used to improve this very promising analysis method, which already has a large signal efficiency improvement for WIMP candidates. The next step will be to apply this method to the last CDMS

low-threshold analysis study, which was background limited. This analysis method should be able to improve the results because of the improved background rejection, and therefore increase the experiment's sensitivity.

Bibliography

[1] Planck captures portrait of the young universe, revealing earliest light. *University of Cambridge*, 2013.

[2] Super cryogenic dark matter search, Retrieved: April 1, 2014.

[3] P.A.R. Ade et al. Planck 2013 results. XV. CMB power spectra and likelihood. 2013.

[4] Adam Anderson. Probing light wimps with supercdms. 2014.

[5] J. Billard, F. Mayet, and D. Santos. Markov Chain Monte Carlo analysis to constrain Dark Matter properties with directional detection. *Phys.Rev.*, D83:075002, 2011.

[6] N. W. Boggess, J. C. Mather, R. Weiss, C. L. Bennett, E. S. Cheng, E. Dwek, S. Gulkis, M. G. Hauser, M. A. Janssen, T. Kelsall, S. S. Meyer, S. H. Moseley, T. L. Murdock, R. A. Shafer, R. F. Silverberg, G. F. Smoot, D. T. Wilkinson, and E. L. Wright. The COBE mission - Its design and performance two years after launch. *apj*, 397:420–429, October 1992.

[7] Y. Coadou. *Shool of Statistis 2008.*

[8] J. Beringer et al. *The Review of Particle Physics.*

[9] Jeffrey Filippini. *A Search for WIMP Dark Matter Using the First Five-Tower Run of the Cryogenic Dark Matter Search.* PhD thesis, University of California, Berkeley, 2008.

[10] S.A. Hertel and M. Pyle. Phonon Pulse Shape Discrimination in SuperCDMS Soudan. 2011.

[11] Scott Hertel. *Advancing the Search for Dark Matter: from CDMS II to SuperCDMS.* PhD thesis, Massachusetts Institute of Technology, 2012.

[12] F. Schwabel. *Advanced Quantum Mechanics, 4th Ed.*

[13] S. van den Bergh. The Early History of Dark Matter. *PASP*, 111:657–660, June 1999.